The Astrophysical Journal, 941:165 (19pp), 2022 December 20

© 2022. The Author(s). Published by the American Astronomical Society.

OPEN ACCESS

https://doi.org/10.3847/1538-4357/aca01e

Photometric and Spectroscopic Study of the EXor-like Eruptive Young Star Gaia19fct

Sunkyung Park[1,2] , Ágnes Kóspál[1,2,3,4] , Péter Ábrahám[1,2,4] , Fernando Cruz-Sáenz de Miera[1,2] , Eleonora Fiorellino[1,2,5] ,
Michał Siwak[1,2] , Zsófia Nagy[1,2] , Teresa Giannini[6] , Roberta Carini[6] , Zsófia Marianna Szabó[1,2,7,8] , Jeong-Eun Lee[9] ,
Jae-Joon Lee[10] , Fabrizio Vitali[6] , Mária Kun[1,2] , Borbála Cseh[1,2,11] , Máté Krezinger[1,2] , Levente Kriskovics[1,2] ,
András Ordasi[1,2] , András Pál[1,2] , Róbert Szakáts[1,2] , Krisztián Vida[1,2] , and József Vinkó[1,2]

[1] Konkoly Observatory, Research Centre for Astronomy and Earth Sciences, Eötvös Loránd Research Network (ELKH), Konkoly-Thege Miklós út 15-17, 1121 Budapest, Hungary; sunkyung.park@csfk.hu
[2] CSFK, MTA Centre of Excellence, Konkoly-Thege Miklós út 15-17, 1121 Budapest, Hungary
[3] Max Planck Institute for Astronomy, Königstuhl 17, D-69117 Heidelberg, Germany
[4] ELTE Eötvös Loránd University, Institute of Physics, Pázmány Péter sétány 1/A, 1117 Budapest, Hungary
[5] INAF-Osservatorio Astronomico di Capodimonte, via Moiariello 16, I-80131 Napoli, Italy
[6] INAF-Osservatorio Astronomico di Roma, Via Frascati 33, I-00078 Monte Porzio Catone, Italy
[7] Max-Planck-Institute für Radioastronomie, Auf dem Hügel 69, D-53121 Bonn, Germany
[8] Scottish Universities Physics Alliance (SUPA), School of Physics and Astronomy, University of St Andrews, North Haugh, St Andrews, KY16 9SS, UK
[9] Department of Physics and Astronomy, Seoul National University, 1 Gwanak-ro, Gwanak-gu, Seoul 08826, Republic of Korea
[10] Korea Astronomy and Space Science Institute 776, Daedeok-daero, Yuseong-gu, Daejeon, 34055, Republic of Korea
[11] MTA-ELTE Lendület "Momentum" Milky Way Research Group, Hungary
Received 2022 September 2; revised 2022 October 28; accepted 2022 November 2; published 2022 December 20

Abstract

Gaia19fct is one of the Gaia-alerted eruptive young stars that has undergone several brightening events. We conducted monitoring observations using multifilter optical and near-infrared photometry, as well as near-infrared spectroscopy, to understand the physical properties of Gaia19fct and investigate whether it fits into the historically defined two classes. We present the analyses of light curves, color variations, spectral lines, and CO modeling. The light curves show at least five brightening events since 2015, and the multifilter color evolutions are mostly gray. The gray evolution indicates that bursts are triggered by mechanisms other than extinction. Our near-infrared spectra exhibit both absorption and emission lines and show time variability throughout our observations. We found lower rotational velocity and lower temperature from the near-infrared atomic absorption lines than from the optical lines, suggesting that Gaia19fct has a Keplerian rotating disk. The CO overtone features show a superposition of absorption and emission components, which is unlike other young stellar objects. We modeled the CO lines, and the result suggests that the emission and absorption components are formed in different regions. We found that although Gaia19fct exhibits characteristics of both types of eruptive young stars, FU Orionis–type objects and EX Lupi–type objects, it shows more similarity with EXors in general.

Unified Astronomy Thesaurus concepts: FU Orionis stars (553); Young stellar objects (1834); Circumstellar disks (235); Multi-color photometry (1077); High resolution spectroscopy (2096); Light curves (918)

1. Introduction

Most young stellar objects (YSOs) exhibit photometric variations in the optical and infrared on various timescales (Carpenter et al. 2001; Megeath et al. 2012; Cody et al. 2014; Park et al. 2021b). The photometric variability of YSOs can be caused by changing accretion rate, varying line-of-sight extinction, or rotating accretion hot or cold spots (Carpenter et al. 2001; Megeath et al. 2012; Kraus et al. 2016; Fischer et al. 2022). Among these photometric variability mechanisms, eruptive YSOs show the most dramatic change in brightness of about 3–6 mag caused by an enhanced mass accretion rate from the disk to the central protostar. Such brightenings are thought to be observable evidence of episodic accretion and a possible solution to the protostellar luminosity problem (Kenyon et al. 1990; Dunham et al. 2010), which is a discrepancy between the luminosity expected by a standard accretion model (Shu 1977) and the observed luminosities of YSOs. Targets showing such a sudden brightness change are historically classified into two

categories (Fischer et al. 2022, and references therein): FU Orionis–type objects (FUors; Herbig 1977) and EX Lupi–type objects (EXors; Herbig 1989).

FUors exhibit a large amplitude of outburst ($\Delta V > 4$ mag) and last for several decades to centuries. Spectroscopically, FUors show mostly absorption-line profiles formed by a hotter disk midplane and have wavelength-dependent spectral types: F–G type in optical and K–M type in near-infrared (NIR; Hartmann & Kenyon 1996; Audard et al. 2014; Connelley & Reipurth 2018; Fischer et al. 2022). EXors have recurrent outbursts with typically smaller amplitude ($\Delta V = 1$–4 mag) that last for several months to years and have an emission-line-dominated spectrum formed by magnetospheric accretion funnels (Herbig 2007; Audard et al. 2014; Hartmann et al. 2016; Fischer et al. 2022).

Recent studies (Fischer et al. 2022, and references therein) show that many of the eruptive young stars have peculiar properties in photometry and spectroscopy, making it difficult to classify into only two classes. Therefore, a detailed study of each eruptive star is important to understand episodic accretion. Thanks to the whole-sky monitoring of the Gaia space mission and its Gaia Photometric Science Alerts Program[12]

Original content from this work may be used under the terms of the Creative Commons Attribution 4.0 licence. Any further distribution of this work must maintain attribution to the author(s) and the title of the work, journal citation and DOI.

---

[12] http://gsaweb.ast.cam.ac.uk/alerts/home

(Hodgkin et al. 2021), which announces targets that show an abrupt brightening or fading, the number of eruptive young stars has been increasing. These discoveries have been classified as FUors (Gaia17bpi, Hillenbrand et al. 2018; Gaia18dvy, Szegedi-Elek et al. 2020), EXors (Gaia18dvz, Hodapp et al. 2019; Gaia20eae, Cruz-Sáenz de Miera et al. 2022a; Ghosh et al. 2022), and in between (Gaia19ajj, Hillenbrand et al. 2019; Gaia19bey, Hodapp et al. 2020).

Gaia19fct (also known as iPTF 15afq) was discovered on 2015 March 13 ($\Delta R \sim 2.5$ mag; Miller et al. 2015), and the outbursting optical spectrum showed rich emission lines. Based on the amplitude of its brightening and rich emission lines, Gaia19fct was suggested as a new EXor (Miller et al. 2015). Repeated brightenings in 2018 and 2019 were reported by Hillenbrand (2019). The brightening in 2019 ($\Delta G > 4$ mag) was reported by the Gaia Photometric Science Alerts Program on 2019 November 14. Giannini et al. (2022) presented optical and NIR spectra of Gaia19fct. The quiescent spectrum is dominated by emission lines, while the outburst spectrum is dominated by absorption lines (Hillenbrand 2019; Giannini et al. 2022). The overall amplitudes, timescales of brightness events, and spectroscopic properties of Gaia19fct are more similar to EXors.

In this study, we present the results of our monitoring program for this target, which started in 2016 September and included photometry and spectroscopy in optical and NIR. We characterize the physical properties of Gaia19fct by analyzing the results of our observational campaigns. Our observations, data reduction, and the used public domain data are described in Section 2. We discuss the environment of Gaia19fct in Section 3. The classification of Gaia19fct and the analyses of photometry and spectroscopy are presented in Section 4. In Section 5, we discuss our results and compare them with previous studies. Finally, we summarize our results and findings in Section 6.

2. Observation

2.1. Photometry

2.1.1. Optical Photometry

We have been monitoring Gaia19fct since 2020 October with the 80 cm Ritchey–Chrétien (RC80) telescope at the Piszkéstető mountain station of Konkoly Observatory in Hungary. The telescope is equipped with an FLI PL230 CCD camera, $0\farcs55$ pixel scale, $18\farcm8 \times 18\farcm8$ field of view, and Johnson V and Sloan $g'r'i'$ filters. After standard bias, dark, and flat-field correction, we co-added the three images per filter per night. We obtained aperture photometry in the co-added images for Gaia19fct and for 40 comparison stars within $10'$ of the science target. We used an aperture radius of 5 pixels ($2\farcs75$) and sky annulus between 20 and 40 pixels ($11''$ and $22''$). We used the APASS9 magnitudes (Henden et al. 2015) of the comparison stars for photometric calibration by fitting a linear color term. The results are listed in Table 1.

2.1.2. Near-infrared Photometry

We obtained photometric images on 2022 March 17 (Program ID: 65-111; PI: Cruz-Sáenz de Miera) using the H and K_s filters of the NOTCam installed at the 2.56 m Nordic Optical Telescope (NOT) located at Roque de los Muchachos Observatory (La Palma, Canary Islands, Spain). For each filter, we used a five-point dither pattern with offsets of $60''$. The exposure time was 4 s in both filters. We constructed sky images by computing the median of the individual frames per filter, and we subtracted it from the original frames (in the K_s band, only four frames were used owing to an instrumental artifact). Flat-field measurements were obtained by the observatory on the same night. For photometric calibration, we used all Two Micron All Sky Survey (2MASS) sources detected in the frames brighter than 13.8 mag (H band) or 13.0 mag (K_s band) and that have a good-quality flag of "A." We determined the calibration factor (the difference between the 2MASS and instrumental magnitudes) by averaging $5-17$ stars, and we applied this factor to Gaia19fct. The influence of intrinsically variable comparison stars was minimized by using an outlier-resistant averaging method. We performed photometry on the individual frames and averaged the results, which also provided formal uncertainties of the final photometric values as the standard deviation of the individual photometric values.

The JHK_s photometric monitoring was carried out between 2016 September and 2022 March with the 60 cm robotic Rapid Eye Mount (REM) telescope (Zerbi et al. 2001), an Italian INAF facility located in La Silla (Chile), hosted by ESO. The NIR images were obtained with the infrared imaging camera REMIR (Vitali et al. 2003, 2006) with broadband J, H, and K_s filters. All the observations were obtained by dithering the field of view around the pointed position, with a total exposure time of 15 s in each band. The raw frames were reduced using the Riace semiautomatic IRAF procedure (F. Vitali et al. 2022, in preparation), which uses the 2MASS catalog to define the average zero-point for the photometric calibration and performs aperture photometry to extract the magnitude of the source in each band. Observing results are listed in Table 1.

2.1.3. Public Domain Data

To get an insight into the historical light variations of Gaia19fct in optical bands, we downloaded all individual Pan-STARRS (Chambers et al. 2016) images containing our target and analyzed them with DAOPHOT procedures available within `astro-idl`. Due to the nearby companion (see more details in Section 3.2), we used a small 5-pixel aperture, which equals $2\farcs25$ in the sky. We stress that this approach may occasionally slightly decrease (by 20%) the total flux obtained from images taken during poor seeing conditions. Fortunately, these losses are small enough and isolated in time and do not affect our general conclusions regarding the large-scale historical variability. The magnitudes were calibrated to the standard system employing the nightly zero-points provided in the fits headers. We checked that the gri bands magnitudes of the three nearby standard stars from the APASS9 (Henden et al. 2015) catalog are in good agreement (± 0.07 mag) with our determinations. The results are listed in Table 2.

Furthermore, we gathered public domain photometry data from various sources to complement our monitoring data. We used Gaia G-band photometry from the Gaia Photometric Science Alerts database and Zwicky Transient Facility (ZTF; Masci et al. 2019) DR13 g- and r-band photometry from the ZTF archive. We used the ZTF data with "catflags = 0," i.e., perfectly clean extracted, to filter out bad-quality images. We also collected VRI bands data from the Hunting Outbursting Young Stars with the Centre of Astrophysics and Planetary Science (HOYS-CAPS[13]) citizen science project run by the

---
[13] http://astro.kent.ac.uk/HOYS-CAPS/

Table 1
Our Optical and NIR Photometry

JD	Date (UT)	g'	V	r'	i'	J	H	K_s	Instrument
2457649.00	2016-09-17	⋯	⋯	⋯	⋯	13.32 ± 0.08	11.85 ± 0.11	10.61 ± 0.10	REMIR
2457664.00	2016-10-02	⋯	⋯	⋯	⋯	14.56 ± 0.13	12.83 ± 0.10	11.31 ± 0.10	REMIR
2457682.00	2016-10-20	⋯	⋯	⋯	⋯	14.47 ± 0.15	12.75 ± 0.11	11.35 ± 0.21	REMIR
2457697.00	2016-11-04	⋯	⋯	⋯	⋯	14.45 ± 0.13	12.57 ± 0.09	10.90 ± 0.08	REMIR
2457713.00	2016-11-20	⋯	⋯	⋯	⋯	13.80 ± 0.10	12.17 ± 0.09	11.50 ± 0.03	REMIR
2457729.00	2016-12-06	⋯	⋯	⋯	⋯	13.20 ± 0.14	11.78 ± 0.22	10.37 ± 0.15	REMIR
2457744.00	2016-12-21	⋯	⋯	⋯	⋯	⋯	11.73 ± 0.12	10.55 ± 0.14	REMIR
2457759.00	2017-01-05	⋯	⋯	⋯	⋯	13.27 ± 0.17	12.08 ± 0.08	10.60 ± 0.18	REMIR
2457774.00	2017-01-20	⋯	⋯	⋯	⋯	13.25 ± 0.12	11.81 ± 0.24	10.76 ± 0.21	REMIR
2457792.00	2017-02-07	⋯	⋯	⋯	⋯	13.66 ± 0.13	12.14 ± 0.22	11.66 ± 0.09	REMIR
2457815.00	2017-03-02	⋯	⋯	⋯	⋯	14.03 ± 0.18	12.47 ± 0.18	11.15 ± 0.14	REMIR
2457891.00	2017-05-17	⋯	⋯	⋯	⋯	14.08 ± 0.11	12.72 ± 0.05	11.63 ± 0.06	REMIR
2457907.00	2017-06-02	⋯	⋯	⋯	⋯	14.10 ± 0.20	⋯	⋯	REMIR
2457908.00	2017-06-03	⋯	⋯	⋯	⋯	⋯	12.86 ± 0.10	11.83 ± 0.11	REMIR
2457991.00	2017-08-25	⋯	⋯	⋯	⋯	14.13 ± 0.11	12.68 ± 0.07	12.05 ± 0.13	REMIR
2458008.00	2017-09-11	⋯	⋯	⋯	⋯	14.08 ± 0.14	12.83 ± 0.15	11.96 ± 0.12	REMIR
2458187.00	2018-03-09	⋯	⋯	⋯	⋯	14.29 ± 0.15	12.99 ± 0.19	12.10 ± 0.10	REMIR
2458202.00	2018-03-24	⋯	⋯	⋯	⋯	13.90 ± 0.12	12.47 ± 0.14	11.45 ± 0.20	REMIR
2458217.00	2018-04-08	⋯	⋯	⋯	⋯	11.71 ± 0.04	10.39 ± 0.03	9.25 ± 0.02	REMIR
2458236.00	2018-04-27	⋯	⋯	⋯	⋯	11.79 ± 0.10	10.37 ± 0.15	9.30 ± 0.18	REMIR
2458251.00	2018-05-12	⋯	⋯	⋯	⋯	11.99 ± 0.07	10.62 ± 0.05	9.50 ± 0.08	REMIR
2458346.00	2018-08-15	⋯	⋯	⋯	⋯	14.39 ± 0.15	⋯	⋯	REMIR
2458350.00	2018-08-19	⋯	⋯	⋯	⋯	14.28 ± 0.18	12.72 ± 0.11	10.98 ± 0.03	REMIR
2458351.00	2018-08-20	⋯	⋯	⋯	⋯	14.48 ± 0.16	12.83 ± 0.08	11.13 ± 0.10	REMIR
2458369.00	2018-09-07	⋯	⋯	⋯	⋯	13.98 ± 0.12	12.32 ± 0.08	10.93 ± 0.07	REMIR
2458385.00	2018-09-23	⋯	⋯	⋯	⋯	13.76 ± 0.18	⋯	10.88 ± 0.05	REMIR
2459145.60	2020-10-23	19.72 ± 0.24	18.61 ± 0.16	17.54 ± 0.08	16.42 ± 0.04	⋯	⋯	⋯	RC80
2459154.66	2020-11-01	19.58 ± 0.25	18.35 ± 0.10	17.87 ± 0.07	16.55 ± 0.03	⋯	⋯	⋯	RC80
2459161.59	2020-11-08	19.86 ± 0.15	19.06 ± 0.13	17.77 ± 0.06	16.75 ± 0.05	⋯	⋯	⋯	RC80
2459175.62	2020-11-22	20.11 ± 0.22	19.27 ± 0.19	17.88 ± 0.08	16.73 ± 0.05	⋯	⋯	⋯	RC80
2459491.61	2021-10-04	18.70 ± 0.06	17.77 ± 0.04	16.59 ± 0.03	15.51 ± 0.03	⋯	⋯	⋯	RC80
2459524.61	2021-11-06	⋯	⋯	16.95 ± 0.05	15.82 ± 0.05	⋯	⋯	⋯	RC80
2459535.54	2021-11-17	20.36 ± 0.39	19.24 ± 0.23	18.07 ± 0.12	16.50 ± 0.07	⋯	⋯	⋯	RC80
2459542.58	2021-11-24	21.50 ± 0.38	20.07 ± 0.19	18.66 ± 0.08	17.27 ± 0.05	⋯	⋯	⋯	RC80
2459546.00	2021-11-27	⋯	⋯	⋯	⋯	13.40 ± 0.12	11.73 ± 0.05	10.20 ± 0.14	REMIR
2459548.54	2021-11-30	20.93 ± 0.27	19.72 ± 0.16	18.86 ± 0.09	17.35 ± 0.04	⋯	⋯	⋯	RC80
2459552.53	2021-12-04	20.66 ± 0.13	19.77 ± 0.13	18.61 ± 0.05	17.15 ± 0.04	⋯	⋯	⋯	RC80
2459556.53	2021-12-08	20.76 ± 0.15	20.02 ± 0.15	18.48 ± 0.06	17.16 ± 0.05	⋯	⋯	⋯	RC80
2459562.49	2021-12-13	20.73 ± 0.16	19.61 ± 0.10	18.37 ± 0.05	16.84 ± 0.04	⋯	⋯	⋯	RC80
2459566.48	2021-12-17	⋯	20.60 ± 0.60	18.44 ± 0.11	17.09 ± 0.08	⋯	⋯	⋯	RC80
2459574.00	2021-12-25	⋯	⋯	⋯	⋯	13.04 ± 0.14	11.43 ± 0.13	10.39 ± 0.26	REMIR
2459581.56	2022-01-02	21.26 ± 0.25	19.64 ± 0.12	18.30 ± 0.06	17.11 ± 0.05	⋯	⋯	⋯	RC80
2459590.00	2022-01-10	⋯	⋯	⋯	⋯	13.32 ± 0.15	11.64 ± 0.15	10.68 ± 0.07	REMIR
2459607.00	2022-01-27	⋯	⋯	⋯	⋯	13.29 ± 0.19	11.92 ± 0.06	10.63 ± 0.16	REMIR
2459614.28	2022-02-03	21.79 ± 1.19	19.61 ± 0.33	18.39 ± 0.20	17.41 ± 0.08	⋯	⋯	⋯	RC80
2459622.00	2022-02-11	⋯	⋯	⋯	⋯	13.62 ± 0.16	12.25 ± 0.24	10.95 ± 0.11	REMIR
2459656.41	2022-03-17	⋯	⋯	⋯	⋯	⋯	11.77 ± 0.04	10.48 ± 0.01	NOTCam
2459668.00	2022-03-29	⋯	⋯	⋯	⋯	13.20 ± 0.12	11.92 ± 0.06	⋯	REMIR
2459857.65	2022-10-05	⋯	⋯	⋯	18.20 ± 0.13	⋯	⋯	⋯	RC80

University of Kent (Froebrich et al. 2018; Evitts et al. 2020). We used the photometric data available from their websites for the Gaia, ZTF, and HOYS-CAPS surveys; therefore, instead of providing their values in the table, we plotted them in Figures 3 and 4.

We downloaded 3.4 μm (W1) and 4.6 μm (W2) photometry for Gaia19fct from the catalogs of the WISE Cryogenic Survey, the NEOWISE Post-Cryo Survey, and the NEOWISE Reactivation mission (Wright et al. 2010; Mainzer et al. 2011, 2014). We used the AllWISE Multiepoch Photometry Table and the NEOWISE-R Single Exposure (L1b) Source Table available at the NASA/IPAC Infrared Science Archive. After filtering for bad-quality data (using the qi_fact, saa_sep, and moon_masked

flags; for more details, see Section II.3.a of the NEOWISE Explanatory Supplement), we applied saturation correction using the appropriate correction curves provided by the NEOWISE Explanatory Supplement (Section II.1.c.iv.a). Finally, we calculated seasonal averages, as WISE typically scanned the sky twice per year. Table 3 lists these averaged WISE magnitudes for Gaia19fct.

2.2. Near-infrared Spectroscopy

2.2.1. IGRINS

NIR spectra of Gaia19fct were obtained with the Immersion GRating INfrared Spectrograph (IGRINS) installed on

Table 2
Pan-STARRS Photometry of Gaia19fct and Its Companion

JD	Date (UT)	Gaia19fct	Companion	Filter
2455593.93	2011-02-01	22.20 ± 0.20	21.99 ± 0.17	g
2455594.82	2011-02-02	22.12 ± 0.18	22.14 ± 0.18	g
2455594.83	2011-02-02	22.54 ± 0.27	22.52 ± 0.26	g
2455948.89	2012-01-22	22.20 ± 0.24	22.09 ± 0.22	g
2455957.97	2012-01-31	22.04 ± 0.17	22.63 ± 0.27	g
2456000.78	2012-03-14	22.36 ± 0.22	22.01 ± 0.17	g
2456358.79	2013-03-07	22.83 ± 0.37	22.06 ± 0.19	g
2456737.77	2014-03-21	21.89 ± 0.17	22.03 ± 0.20	g
2456737.78	2014-03-21	22.39 ± 0.28	22.50 ± 0.31	g
2455587.92	2011-01-26	20.63 ± 0.06	21.06 ± 0.07	r
2455940.85	2012-01-14	19.40 ± 0.02	20.93 ± 0.06	r
2455940.86	2012-01-14	19.42 ± 0.02	20.97 ± 0.07	r
2456000.79	2012-03-14	20.14 ± 0.04	20.92 ± 0.07	r
2456000.80	2012-03-14	20.24 ± 0.05	20.98 ± 0.07	r
2456601.13	2013-11-04	19.60 ± 0.03	21.05 ± 0.08	r
2456676.89	2014-01-19	19.98 ± 0.05	20.89 ± 0.10	r
2456676.91	2014-01-19	20.05 ± 0.06	20.97 ± 0.10	r
2456709.78	2014-02-21	20.96 ± 0.09	⋯	r
2455194.99	2009-12-29	19.42 ± 0.04	19.49 ± 0.04	i
2455195.00	2009-12-29	19.46 ± 0.04	19.46 ± 0.04	i
2455584.83	2011-01-23	19.82 ± 0.06	19.45 ± 0.04	i
2455584.84	2011-01-23	19.74 ± 0.05	19.43 ± 0.04	i
2455584.86	2011-01-23	19.78 ± 0.05	19.39 ± 0.04	i
2455584.87	2011-01-23	19.67 ± 0.05	19.43 ± 0.04	i
2455940.87	2012-01-14	17.83 ± 0.01	⋯	i
2455957.89	2012-01-31	18.95 ± 0.02	19.35 ± 0.02	i
2455957.90	2012-01-31	18.93 ± 0.02	19.33 ± 0.02	i
2456313.90	2013-01-21	18.59 ± 0.02	19.33 ± 0.03	i
2456313.92	2013-01-21	18.58 ± 0.02	19.29 ± 0.03	i
2456652.98	2013-12-26	18.45 ± 0.01	19.28 ± 0.02	i
2456652.99	2013-12-26	18.53 ± 0.01	19.30 ± 0.02	i
2456734.76	2014-03-18	18.64 ± 0.02	⋯	i
2456734.77	2014-03-18	18.59 ± 0.02	⋯	i
2456734.79	2014-03-18	18.67 ± 0.02	⋯	i
2455283.86	2010-03-28	15.38 ± 0.01	⋯	z
2455283.87	2010-03-28	15.37 ± 0.01	⋯	z
2455503.09	2010-11-02	18.30 ± 0.02	18.84 ± 0.03	z
2455503.10	2010-11-02	18.33 ± 0.02	18.89 ± 0.03	z
2455637.73	2011-03-17	19.86 ± 0.09	19.26 ± 0.04	z
2455637.75	2011-03-17	19.53 ± 0.07	19.34 ± 0.05	z
2455905.03	2011-12-09	16.52 ± 0.01	⋯	z
2455905.05	2011-12-09	16.59 ± 0.01	⋯	z
2456015.75	2012-03-29	17.31 ± 0.01	18.67 ± 0.03	z
2456216.13	2012-10-15	17.81 ± 0.02	⋯	z
2456596.14	2013-10-30	16.80 ± 0.01	18.68 ± 0.02	z
2456641.99	2013-12-15	17.31 ± 0.01	18.76 ± 0.03	z
2455517.11	2010-11-16	17.42 ± 0.02	18.57 ± 0.05	y
2455517.12	2010-11-16	⋯	18.66 ± 0.05	y
2455637.77	2011-03-17	18.91 ± 0.09	18.88 ± 0.08	y
2455852.14	2011-10-17	⋯	18.21 ± 0.04	y
2456014.73	2012-03-28	16.77 ± 0.02	18.54 ± 0.06	y
2456014.74	2012-03-28	16.74 ± 0.02	18.50 ± 0.06	y
2456206.13	2012-10-05	16.96 ± 0.02	18.54 ± 0.06	y
2456206.14	2012-10-05	17.03 ± 0.02	18.53 ± 0.06	y
2456602.15	2013-11-05	16.23 ± 0.01	⋯	y
2456642.02	2013-12-15	16.84 ± 0.02	18.32 ± 0.05	y
2456776.74	2014-04-29	17.03 ± 0.01	18.52 ± 0.04	y
2456943.15	2014-10-12	17.23 ± 0.03	18.62 ± 0.07	y

Table 3
NEOWISE Photometry

JD	Date (UT)	W1	W2
2455292.04	2010-04-05	8.610 ± 0.015	7.513 ± 0.015
2455483.53	2010-10-14	9.911 ± 0.045	8.841 ± 0.044
2456947.14	2014-10-16	11.019 ± 0.018	9.809 ± 0.017
2457115.87	2015-04-03	8.131 ± 0.015	7.062 ± 0.012
2457310.42	2015-10-14	10.449 ± 0.017	9.395 ± 0.015
2457474.94	2016-03-27	10.958 ± 0.019	9.820 ± 0.016
2457674.60	2016-10-13	9.460 ± 0.016	8.270 ± 0.013
2457835.48	2017-03-22	9.752 ± 0.016	8.756 ± 0.014
2458040.37	2017-10-13	10.324 ± 0.017	9.173 ± 0.015
2458196.11	2018-03-18	10.138 ± 0.016	9.017 ± 0.014
2458405.82	2018-10-14	9.314 ± 0.016	8.321 ± 0.013
2458563.12	2019-03-20	10.742 ± 0.018	9.578 ± 0.016
2458770.06	2019-10-13	10.541 ± 0.017	9.274 ± 0.015
2458927.25	2020-03-18	7.545 ± 0.018	6.670 ± 0.013
2459137.15	2020-10-14	9.668 ± 0.017	8.709 ± 0.014
2459292.54	2021-03-19	10.387 ± 0.017	9.377 ± 0.015
2459501.17	2021-10-13	7.928 ± 0.016	6.884 ± 0.012

a single exposure (Yuk et al. 2010; Ramsay et al. 2014; Evans et al. 2016). The spectrum was obtained with a slit scale of $0\rlap{.}''34 \times 5''$. The signal-to-noise ratios (S/Ns) of H and K bands on November 19 are ∼190 and ∼270 and on November 23 are ∼137 and ∼201, respectively. Gaia19fct was observed with several series of ABBA nodding observations at different positions on the slit to subtract the sky background. The exposure time of each nod observation was 300 s, and the total exposure times for 2020 November 19 and 23 were 3600 and 2400 s, respectively. Nearby A0 telluric standard stars (HIP 31226 and HIP 29933) were observed immediately after or before the observation of Gaia19fct for telluric correction.

The data reduction was done using the IGRINS pipeline (Lee & Gullikson 2017) for flat-fielding, sky subtraction, correcting the distortion of the dispersion direction, wavelength calibration, and combining the spectra. Then, telluric correction was performed in the same manner as done in Park et al. (2018). For flux calibration, interpolated H- and K-band magnitudes between our RC80 $gVri$ bands and NEOWISE data observed on 2020 November 22 and 2020 October 14 were adopted since there is no recent NIR photometry close to the observing date. The barycentric velocity (V_{bary}) was calculated by barycorrpy (Kanodia & Wright 2018), which is 20.22 and 19.12 km s^{-1} for November 19 and 23, respectively. The systemic velocity ($V_{\mathrm{LSR}} = 13.25$ km s^{-1}) obtained from APEX ^{13}CO 3 − 2 data (Cruz-Sáenz de Miera et al. 2022b) is converted into the heliocentric system ($V_{\mathrm{helio}} = 31.41$ km s^{-1}) and used for the velocity correction. Finally, the V_{bary} and systemic velocity (V_{helio}) correction was applied.

2.2.2. NOTCam

The intermediate-resolution ($R = 2500$) H- and K-band spectra of Gaia19fct were acquired with NOTCam on the NOT on 2022 March 17 (Program ID: 65-111; PI: Cruz-Sáenz de Miera). Gaia19fct was observed with an ABABAB pattern with exposure time of 210 and 294 s for H and K bands, respectively. The full pattern was observed twice for the K band; thus, the total exposure times for the H and K bands are 1260 and 3528 s, respectively. The nearby telluric

the 8.1 m Gemini South telescope on 2020 November 19 and 23 (Program ID: GS-2020B-Q-218; PI: Park). IGRINS provides high-resolution ($R = 45,000$) NIR spectra covering the full H (1.49–1.80 μm) and K (1.96–2.46 μm) bands with

Table 4
Spectroscopic Observing Log

Target	JD	Date (UT)	Band	Exp. Time (s)	Instrument
Gaia19fct	2459172.79	2020-11-19	H, K	300×12	IGRINS
HIP 31226[a]	2459172.84	2020-11-19	H, K	26×4	IGRINS
Gaia19fct	2459176.78	2020-11-23	H, K	300×8	IGRINS
HIP 29933[a]	2459176.76	2020-11-23	H, K	42×10	IGRINS
Gaia19fct	2459656.38	2022-03-17	H	210×6	NOTCam
Gaia19fct	2459656.43	2022-03-17	K	294×12	NOTCam
HD 44037[b]	2459656.36	2022-03-17	H, K	10×4	NOTCam

Notes.
[a] Telluric standard star (A0 V) was observed right after or before the target to correct the telluric absorption features.
[b] Telluric standard star (B9 V) was observed right before the target to correct the telluric absorption features.

standard star HD 44037 (B9 V) was observed right before the target observation for telluric correction. The spectroscopic observing log is listed in Table 4. The S/Ns of H- and K-band spectra around 1.6 and 2.2 μm are ~24 and ~20, respectively.

The raw data were reduced using IRAF (Tody 1986) for sky subtraction, flat-fielding, bad-pixel removal, aperture tracing, and wavelength calibration. A xenon lamp spectrum was used for the wavelength calibration. Hydrogen lines in the HD 44037 spectrum were removed, and then the spectrum was normalized. The target spectrum was divided by the normalized telluric spectrum to correct for the telluric lines. We used the H and K magnitudes observed with NOTCam on the same date for flux calibration. The V_{bary} was calculated by barycorrpy (Kanodia & Wright 2018) as -23.07 km s^{-1}, and barycentric and systemic velocity correction ($V_{\text{helio}} = 31.41$ km s^{-1}) was applied.

3. Gaia19fct

3.1. Location

Gaia19fct ($\alpha_{\text{J2000}} = 07^{\text{h}} 09^{\text{m}} 21\overset{\text{s}}{.}39$, $\delta_{\text{J2000}} = -10° 29' 34\overset{''}{.}55$) is located close to the Galactic plane ($l = 224.30051$, $b = -0.84175$) and lies toward the Canis Major OB1 (CMa OB1) association. According to Sewiło et al. (2019), Gaia19fct belongs to the "CMa$-l$224" region (centered at (l, b) = (224.5, -0.65); see their Figures 3 and 4), where young protostars with outflows are found. The median kinematic distance using the ^{12}CO $1-0$ data is 0.92 kpc, and about 99% of targets in the CMa–l224 region are located between 0.5 and 1.3 kpc distance (Sewiło et al. 2019). This kinematic distance agrees with the Gaia DR2 distance of $1.14^{+1.01}_{-0.38}$ kpc provided by Bailer-Jones et al. (2018) and 1.32 ± 0.44 kpc calculated using the Gaia DR3 parallax (Gaia Collaboration et al. 2022), within the uncertainties. Gaia DR3 provides the distance of Gaia19fct as $409.70^{+103.25}_{-86.50}$ pc; however, the fractional parallax uncertainty[14] is high (0.34). Therefore, we adopted the kinematic distance of 0.92 kpc (Sewiło et al. 2019), which is consistent with Gaia DR2 (Bailer-Jones et al. 2018), Gaia DR3 parallax distance, and previous studies about the distance of CMa OB1 association (Kaltcheva & Hilditch 2000; Gregorio-Hetem 2008), for the analysis in this work.

Figure 1. Pan-STARRS giy color-composite image of Gaia19fct. The image shows a $1' \times 1'$ area centered on Gaia19fct, and the companion is located $2''$ to the west.

3.2. Companion

Figure 1 shows the Pan-STARRS giy color-composite image of Gaia19fct (redder source) and its companion (bluer source). The companion is located ~$2''$ west of the target (~1840 au in projection at a distance of 0.92 kpc), and its coordinates are $\alpha_{\text{J2000}} = 07^{\text{h}} 09^{\text{m}} 21\overset{\text{s}}{.}26$, $\delta_{\text{J2000}} = -10° 29' 34\overset{''}{.}42$ (Gaia DR3 source ID: 3046391410808013696).

We checked the distance of the companion to find out whether it is physically related to Gaia19fct. For this verification, we used the Gaia DR3 data, and the parallax distance of the companion (1.38 ± 1.29 kpc) is similar to that of Gaia19fct (1.32 ± 0.44 kpc), implying that Gaia19fct and the companion may form a physical pair.

We also examined the Pan-STARRS photometry of the companion separately from the target to check whether it contaminates the photometry of Gaia19fct (Table 2). The photometry result was constant within 0.3 mag. In addition, the Gaia G-mag uncertainty versus G-mag graph[15] shows that the companion is stable while Gaia19fct is variable. These results

---

[14] https://gea.esac.esa.int/archive/documentation/GDR3/pdf/GaiaDR3_documentation_1.1.pdf

[15] https://gea.esac.esa.int/archive/documentation/GEDR3/Data_processing/chap_cu5pho/cu5pho_sec_photProc/cu5pho_ssec_photVal.html

confirm that the companion is a stable source, not affecting our light-curve analysis for Gaia19fct.

4. Results and Analysis

4.1. Classification

Gaia19fct was classified as a Class I YSO in the pre-outburst stage based on its spectral energy distribution (SED) and strong infrared excess (Miller et al. 2015). Later, Fischer et al. (2016) also suggested Gaia19fct as Class I based on the infrared colors. Sewiło et al. (2019) fitted the SED with a star and passive disk model and classified it as a disk-only source without an envelope. In order to revisit the evolutionary stage of Gaia19fct, we used several methods: bolometric temperature (T_{bol}), spectral index (α), and infrared colors.

We constructed the SED with several different data sets (Figure 2). First, we gathered the data observed before its discovery in 2015 (gray circles); the data are from Pan-STARRS (PS1; Chambers et al. 2016), 2MASS (Cutri et al. 2003), IRAC (Sewiło et al. 2019), AllWISE (Cutri et al. 2014), AKARI (Ishihara et al. 2010), and PACS 70 μm (Sewiło et al. 2019). The light curves (Figure 3) show at least five burst events, making a plausible assumption that this target had bursts before 2015. Therefore, we constructed additional SEDs based on the light curve. Second, we used the ZTF gr, REM JHK_s, and NEOWISE W1 and W2 data observed in the 2018–2019 quiescent period (pink squares). Third, we collected the data observed in the 2021–2022 period with RC80 $gVri$, Gaia G, REM JHK_s, and WISE W1 and W2, the minimum phase between the two brightenings (blue triangles). Finally, we selected the faintest data (black stars) at each wavelength to assume the quiescent phase of Gaia19fct. The data observed at different epochs show different SED shapes, and we decided to use the 2018–2019 SED, which corresponds to the quiescent phase in the light curve, for the analysis.

We calculated L_{bol} and T_{bol} for the 2018–2019 period, which is assumed to be the quiescent phase, by integrating the SED following the procedure described by Chen et al. (1995). We used WISE W3 and W4 (Cutri et al. 2014) and PACS 70 μm (Sewiło et al. 2019) data for the longer wavelengths because only shorter-wavelength (up to 4.5 μm) data were available. The resulting L_{bol} and T_{bol} are $5.6 \pm 1.6 L_{\odot}$ and 481 ± 10 K, respectively, when assuming a distance of 0.92 kpc. The uncertainty of L_{bol} was estimated using a Markov Chain Monte Carlo approach. First, we created Gaussian distributions of each photometric measurement and the distance to the target, where each one of these distributions was made up of 50,000 elements. We used the values and uncertainties of each photometric point, as well as the distance, to inform the Gaussian mean and width. In the case where we could not obtain an uncertainty to a photometric measurement, we assumed uncertainty of 30%. Second, we computed 50,000 values of L_{bol} using all the Gaussian distributions. Finally, we used this posterior distribution to calculate the 0.16, 0.50, and 0.84 quantiles and thus determine the value of L_{bol} and its uncertainties. Due to the small errors of the photometric points (~2%), we infer that the uncertainty of L_{bol} is dominated by the distance and by the few photometric points with large uncertainties. The uncertainty of T_{bol} was calculated with photometric errors. The calculated T_{bol} is in the range of Class I (70 K $\leqslant T_{bol} \leqslant 650$ K; Chen et al. 1995; Evans et al. 2009), suggesting that Gaia19fct is in the Class I stage. The α of pre-
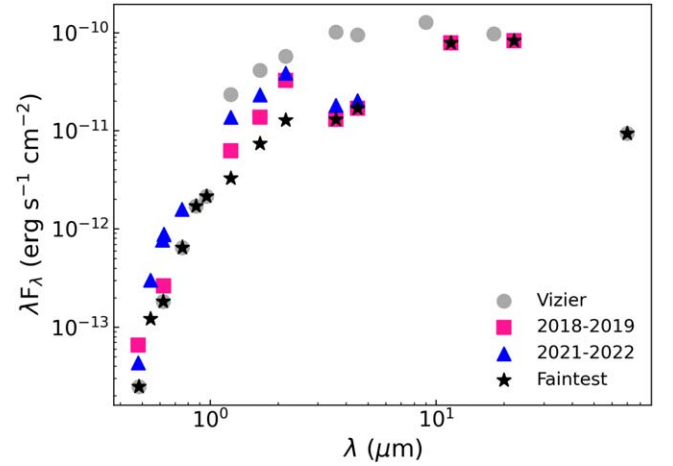

Figure 2. SED of Gaia19fct. Different colors and symbols present different epochs. For the 2018–2019 period, we used the ZTF gr and REM JHK_s observed in 2018 November and August, respectively, and NEOWISE W1 and W2 observed in 2019 March. For the 2021–2022 period, we adopted the RC80 $gVri$, Gaia G, and REM JHK_s observed in 2022 February and NEOWISE W1 and W2 obtained in 2021 March.

outburst SED between 2 and 24 μm has been widely used to classify the evolutionary stage of YSOs (Lada 1987; Evans et al. 2009). The α of Gaia19fct during the quiescent 2018–2019 period is about 0.4, which also corresponds to Class I ($0.3 \leqslant \alpha$; Evans et al. 2009, and references therein).

We also used 2MASS and WISE colors to check the YSO class of Gaia19fct. The MIR bands are related to a cooler circumstellar disk and envelope than the stellar photosphere, making MIR colors a useful indicator for YSO classification. Using these values of Gaia19fct, we found that it falls toward Class I (Koenig & Leisawitz 2014; Fischer et al. 2016). When both 2MASS and WISE colors are used, Gaia19fct falls between Class I and flat spectrum (Koenig & Leisawitz 2014). In addition, the location of Gaia19fct in the W1 − W2 versus W3 − W4 plot is surrounded by Class I and flat-spectrum sources. The evolutionary stage of Gaia19fct varies between Class I and flat spectrum depending on the methods. In this work, we will analyze Gaia19fct as a Class I based on T_{bol} and α.

4.2. Extinction

We estimated an extinction (A_V) by comparing the spectrum of Gaia19fct to that of FU Ori as done in Connelley & Reipurth (2018). FU Ori is known to have a low extinction ($A_V = 1.7$ mag; Siwak et al. 2018; Green et al. 2019; Lykou et al. 2022), making it a good comparison target. This method is valid for eruptive young stars whose optical and NIR spectra are dominated by an active accretion disk rather than the stellar photosphere (Hartmann & Kenyon 1996; Connelley & Reipurth 2018; Fischer et al. 2022). The spectral continuum shape and lines observed in 2020 November are similar to those of FUors. Therefore, we assumed that the continuum shape of Gaia19fct observed in 2020 November is dominated by extinction, rather than the spectral type. The Gaia19fct spectrum was dereddened until it matched with that of FU Ori, and we matched the continuum shape of the spectrum, not the absolute flux level. As a result, we obtained A_V for 2020 November as 8 ± 1 mag.

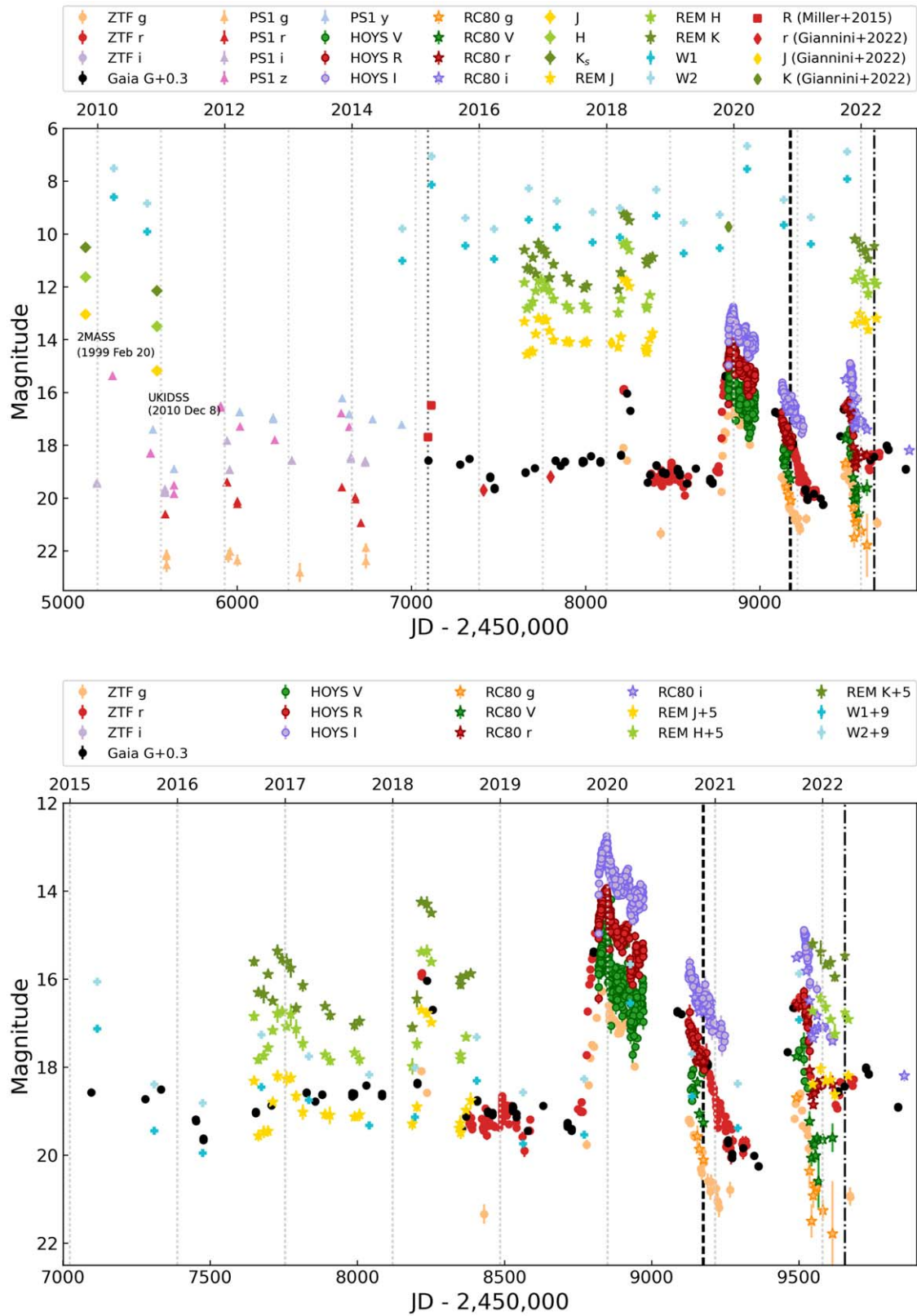Extinction can also be estimated using the ratio of pairs of emission lines that share the same upper energy level

Figure 3. Light curve of Gaia19fct. ZTF (*g*, *r*; Masci et al. 2019), HOYS (*V*, *R*, *I*; Froebrich et al. 2018; Evitts et al. 2020), WISE (W1 and W2; Mainzer et al. 2011), 2MASS (*J*, *H*, *K_s*; Cutri et al. 2003), UKIDSS (*J*, *H*, *K_s*; Lawrence et al. 2007), Pan-STARRS (*g*, *r*, *i*, *z*, *y*; Chambers et al. 2016), and Gaia archives (*G*), as well as our RC80 (*g*, *V*, *r*, *i*) and REM (*J*, *H*, *K_s*) monitoring observation data, are used. Circles and stars represent public domain data and our observations, respectively. Black dashed and dashed–dotted lines indicate IGRINS and NOTCam spectral observing dates, respectively. Uncertainties smaller than the symbol size are not presented.

(Davis et al. 2011, and references therein). Among several lines, only H$_2$ 1–0 $S(1)$/1–0 $Q(3)$ lines were available in our 2020 November observation. The following equation is used to estimate the extinction (Davis et al. 2011):

$$A_V = -114 \times \log(0.704 \times [I_{S1}/I_{Q3}]). \tag{1}$$

The estimated A_V for 2020 November is ~7.0 mag, lower than that of Sewiło et al. (2019) obtained by the SED fitting ($A_V = 10.2$ mag). In order to double-check the obtained A_V, we also used another equation from Petersen & Gammelgaard (1996):

$$A_V = \frac{2.5 \log(R_o/R_p)}{A_{\lambda_2}/A_V - A_{\lambda_1}/A_V}. \tag{2}$$

R_o is the observed line ratio (I_{Q3}/I_{S1}), and R_p is the theoretical line ratio of ~0.7 (Turner et al. 1977). A_{λ_1} and A_{λ_2} are the wavelengths of H$_2$ 1–0 $Q(3)$ and H$_2$ 1–0 $S(1)$, respectively. To calculate A_{λ_1}/A_V and A_{λ_2}/A_V, we used an extinction law from Equation (3) of Rieke & Lebofsky (1985):

$$A_\lambda = A_V (0.55 \, \mu m/\lambda)^{1.6}. \tag{3}$$

The calculated A_V using Equation (2) is ~7.2 mag. The A_V calculated from the H$_2$ line ratio (mean value of the two equations is 7.1 ± 0.2 mag) is lower than the target because H$_2$ lines originate from the jet. Still, this value agrees well with the uncertainty of A_V obtained with spectral comparison ($A_V = 8 \pm 1$ mag). Therefore, we assume that the A_V obtained by comparing with the FU Ori spectrum is from Gaia19fct and use this value ($A_V = 8 \pm 1$ mag) for the analysis.

4.3. Photometry

4.3.1. Light Curve

Figure 3 shows light curves of Gaia19fct. The source has undergone brightening events at least four more times after its first discovery in 2015 (Miller et al. 2015): 2016, 2018, 2019, and 2021. Again, the small brightening event in 2022 March recurred, and the recent data show fading. The amplitude and duration of the 2015, 2016, and 2018 events were moderate ($\lesssim 2.5$ mag) and short-lived, typical of EXors. The 2016 burst ($\Delta V = \sim 1-2.5$ mag; Fischer et al. 2022) was only detected in our NIR observations with an amplitude of about 1 mag ($\Delta J \sim 1.2$ mag, $\Delta H \sim 0.8$ mag, and $\Delta K \sim 0.5$ mag), and the total duration of this event was only about 2 months. Based on the ZTF r-band photometry, the fading rate of the 2018 event is about 0.021 mag day^{-1} during about 170 days with $\Delta r > 3.5$ mag. The amplitude of 2019 brightening is higher than 4.8 mag, the largest burst in Gaia19fct, and is categorized as an outburst ($\Delta V = \sim 2.5-6$ mag; Fischer et al. 2022). The high amplitude is similar to what is typical for FUors (Fischer et al. 2022, and references therein), as well as the most powerful outbursts found in EXors (EX Lup, Ábrahám et al. 2019; Rigliaco et al. 2020; Gaia20eae, Cruz-Sáenz de Miera et al. 2022a; Ghosh et al. 2022). The peak brightness was reached in 2019 December within ~70 days since the beginning of the outburst (2019 October), resulting in a steep rising rate of -0.072 mag day^{-1}. Then, the brightness faded again ($\Delta r > 5.3$ mag) with a rate of 0.015 mag day^{-1} for about 357 days. This target brightened again ($\Delta r > 3.5$ mag) in 2021 April with a rate of -0.019 mag day^{-1} for about 191 days; the peak was in 2021 October ($r = 16.41$ mag), then fading with a rate of 0.044 mag day^{-1} for about 49 days ($\Delta r > 2.15$ mag). Recently, Gaia19fct showed a small brightening variation ($\Delta G = 0.56$ mag) in spring 2022 according to the Gaia G-band and ZTF g- and r-band photometry, and the latest Gaia G-band and RC80 i-band data show fading again ($\Delta G = 0.91$ mag). The amplitude of the latest brightening event is less than the burst defined by Fischer et al. (2022). The amplitudes of the four bursts in 2015, 2016, 2018, and 2021 and one outburst event in 2019 resemble EXors and FUors, respectively. The duration of each event lasts less than a year, which is more similar to EXors. Overall, the moderate amplitudes and short-lived timescales of the bursts of Gaia19fct make it more similar to EXors (Fedele et al. 2007; Fischer et al. 2022).

The WISE light curves show a brightness change trend with a cycle of about 1800 days between 2010 and 2021. The detailed analysis is not possible because of the coarse data coverage, but the brightness peak periods in 2015, 2016, 2020, and 2021 match the optical and NIR light curves. While no contemporary optical or NIR data are available from 2010, the difference between the two WISE observations taken about half a year apart strongly suggests that there was a brightening event also in 2010.

4.3.2. Search for Small-scale Quasi-periodic Light Changes

To get an insight into the small-scale variability, we performed a frequency analysis of the most numerous HOYS RI and ZTF r-band data obtained during the maxima and the fading stages. We aimed to find small-scale periodic or quasi-periodic light variations other than the large-scale ones leading to the major outbursts. Detection of time-coherent small-scale variability can be used to constrain the inner disk dynamic or at least the outer environment in FUors and EXors. The best-established results are usually obtained when the light curves are continuously gathered by a spacecraft (Siwak et al. 2013, 2018, 2020; Hodapp et al. 2019; Szabó et al. 2021), but this kind of analysis is also possible for well-sampled ground-based light curves (Green et al. 2013; Baek et al. 2015; Hackstein et al. 2015; Ghosh et al. 2022).

As a result, we obtained that, except for a few random-like variations directly visible in the light curves, there is no significant variability that would last for at least a few consecutive cycles. This is reminiscent of the situation in V1057 Cyg (Szabó et al. 2021) and V1515 Cyg (Szabó et al. 2022), where the inner disk light is strongly reprocessed by the obscuring surrounding envelope (Szabó et al. 2021).

4.3.3. Color Variation

Figure 4 shows color–magnitude diagrams (CMDs) of Gaia19fct using different photometric bandpasses. The top left panel presents the r versus $g - r$ CMD constructed using ZTF and our RC80 data and shows gray dimming since late 2019. The top right and middle left panels show HOYS V versus $V - I$ and V versus $V - R$ CMDs. In both CMDs, all small color variations seem to follow the extinction path. However, the overall trend from 2019 to 2022 shows gray evolution, which is also seen in the NEOWISE and JHK_s color variations (middle right and bottom panels). The gray variability in the optical and IR suggests that mechanisms other than extinction change cause the color variation of the 2019 and 2021 bursts.
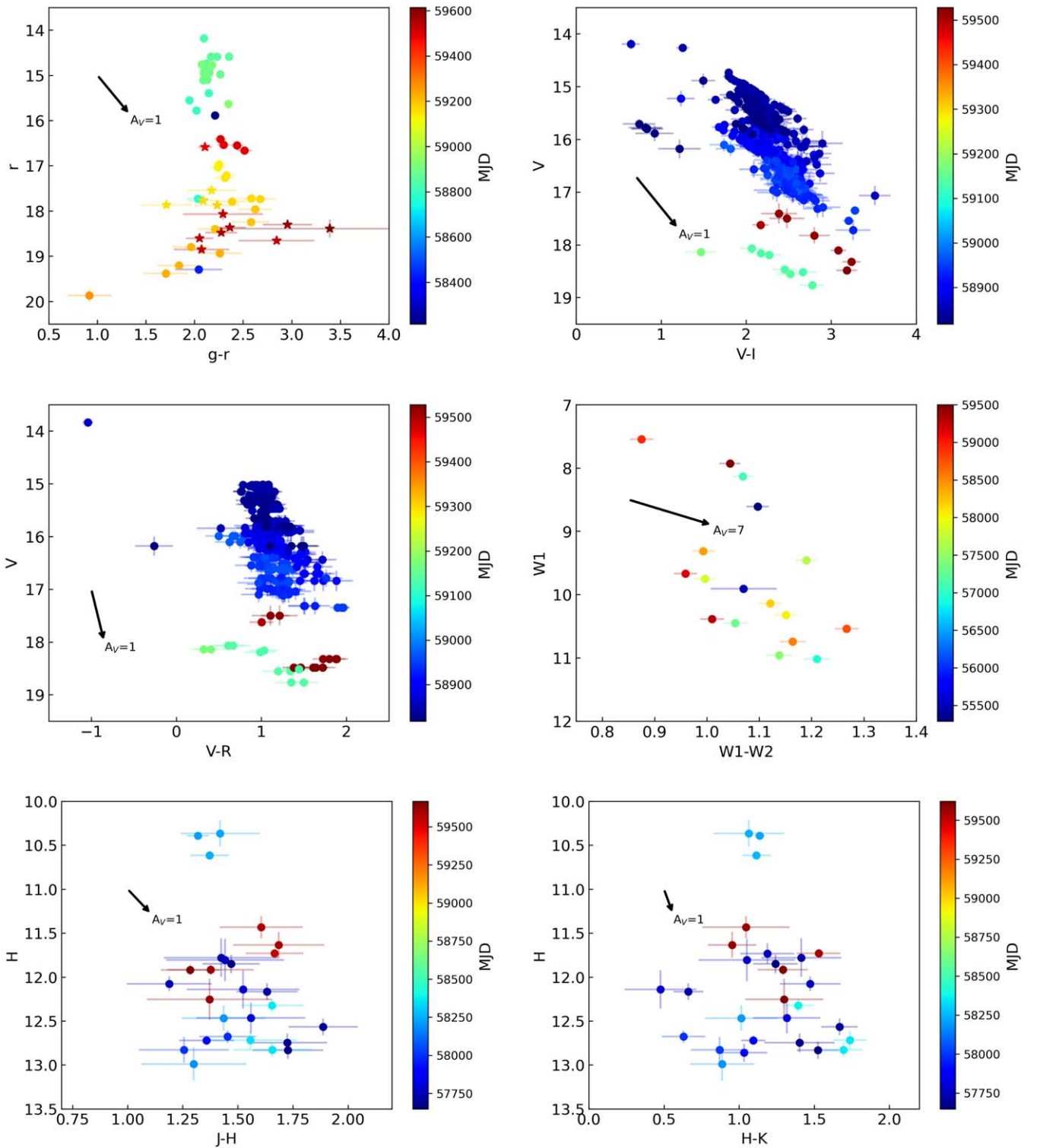
Figure 4. CMDs of Gaia19fct. Top left: r vs. $g - r$ diagram based on the ZTF (circle) and RC80 (star) data. Top right and middle left: V vs. $V - I$ and V vs. $V - R$ diagrams based on HOYS data. Middle right: W1 vs. W1 $-$ W2 diagram based on NEOWISE data. Bottom left and right: REM H vs. $J - H$ and H vs. $H - K$ diagrams.

4.4. Near-infrared Spectroscopy

Figure 5 shows our NIR spectra obtained in 2020 November 19 (black), 2020 November 23 (light gray), and 2022 March 17 (dark gray). In 2020 November, the H-band continuum shape of Gaia19fct is triangular, and the K-band continuum shape is almost flat and decreases from 2.3 μm. The H- and K-band continuum shapes of Gaia19fct are more similar to FUors than FUor-like or peculiar objects (Connelley & Reipurth 2018). In 2022 March, both H- and K-band continua increase toward longer wavelengths, and the steeply rising K-band continuum shape is typical of Class I sources (Beck 2007; Connelley & Greene 2010).
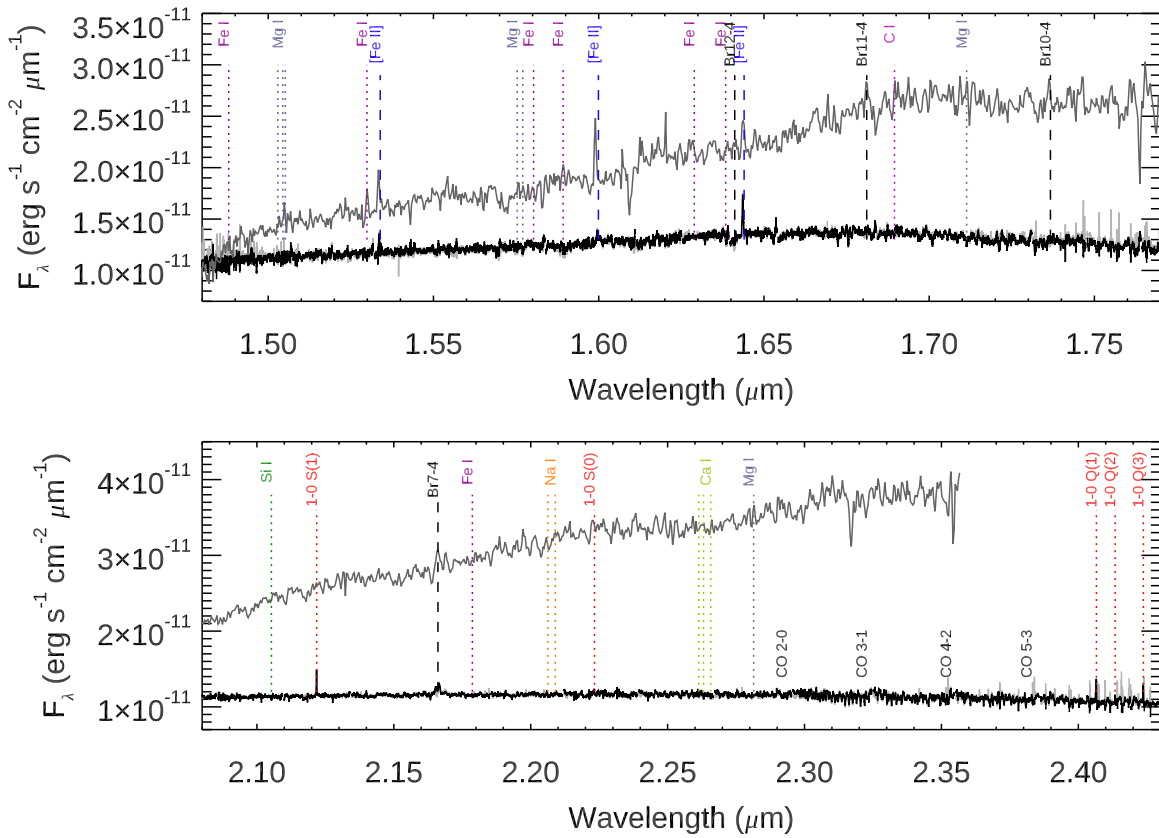
Figure 5. *H*- and *K*-band spectra of Gaia19fct observed on 2020 November 19 (black), 2020 November 23 (light gray), and 2022 March 17 (dark gray). Telluric correction of the second observation (light gray) was not perfect; therefore, emission profiles remained at the edge of each band, especially longer than 2.38 μm. Different colors indicate different spectral lines.

Most FUors show absorption-dominated spectra formed by a viscously heated inner disk midplane (Connelley & Reipurth 2018, and references therein), and only a few FUors show emission lines; see, for example, V2494 Cyg (Magakian et al. 2013), V960 Mon (Takagi et al. 2018; Park et al. 2020), V346 Nor (Kóspál et al. 2020), and V1057 Cyg (Szabó et al. 2021). On the other hand, EXors show emission-dominated spectra formed by a magnetospheric funnel (Fischer et al. 2022, and references therein).

Our NIR spectra show both absorption and emission lines. In our first observation epoch with IGRINS in 2020 November, atomic metal lines are observed in absorption, characteristic of FUors. Several emission lines are also observed, including [Fe II], H$_2$, and Br series, and these lines are associated with jets/outflows and accretion. CO overtone band heads are observed weakly in emission, and the overall CO features show a superposition of emission and absorption. These emission lines are typically observed in EXors or embedded YSOs. The observed absorption and emission lines do not vary in the two observations within 4 days except in the Br series. Therefore, the two IGRINS spectra were combined by observation error weighting to increase the S/N, and the combined spectrum was used for the analysis. The second-epoch observation with NOTCam in 2022 March is dominated by emission lines, including [Fe II] and Br series. In this observation, H$_2$ and CO features are not observed: they may be absent or too weak to be detected. The continuum shapes and spectral lines of the two epochs varied depending on the observation dates. The overall spectral characteristics show similarities with both FUors and EXors.

Table 5
Equivalent Widths

Transition	Wavelength (μm)	EW (2020 November) (Å)	EW (2022 March) (Å)
Br 12–4	1.641	⋯	-0.876 ± 0.177
Br 11–4	1.681	-0.301 ± 0.008[a]	-1.832 ± 0.242
		0.325 ± 0.009[b]	
Br 10–4	1.737	⋯	-2.294 ± 0.319
Br 7–4	2.166	-2.252 ± 0.010[a]	-1.434 ± 0.363
		-1.633 ± 0.012[b]	
CO 2–0	2.293	-0.849 ± 0.022	⋯
1–0 S(3)	1.958	-1.025 ± 0.028	⋯
1–0 S(2)	2.034	-0.176 ± 0.002	⋯
1–0 S(1)	2.122	-0.534 ± 0.002	⋯
1–0 S(0)	2.223	-0.158 ± 0.002	⋯
1–0 Q(1)	2.407	-0.510 ± 0.002	⋯
1–0 Q(2)	2.413	-0.133 ± 0.002	⋯
1–0 Q(3)	2.424	-0.451 ± 0.003	⋯
[Fe II]	1.534	-0.460 ± 0.005	-2.350 ± 0.297
[Fe II]	1.600	-0.334 ± 0.003	-2.074 ± 0.329
[Fe II]	1.644	-1.105 ± 0.003	-0.684 ± 0.185

Notes.
[a] Observed on 2020 November 19.
[b] Observed on 2022 November 23.

4.4.1. Equivalent Width

We measured the equivalent width (EW) of relatively strong and isolated lines to study how the spectral lines changed. Each line was fitted with a Gaussian to define the
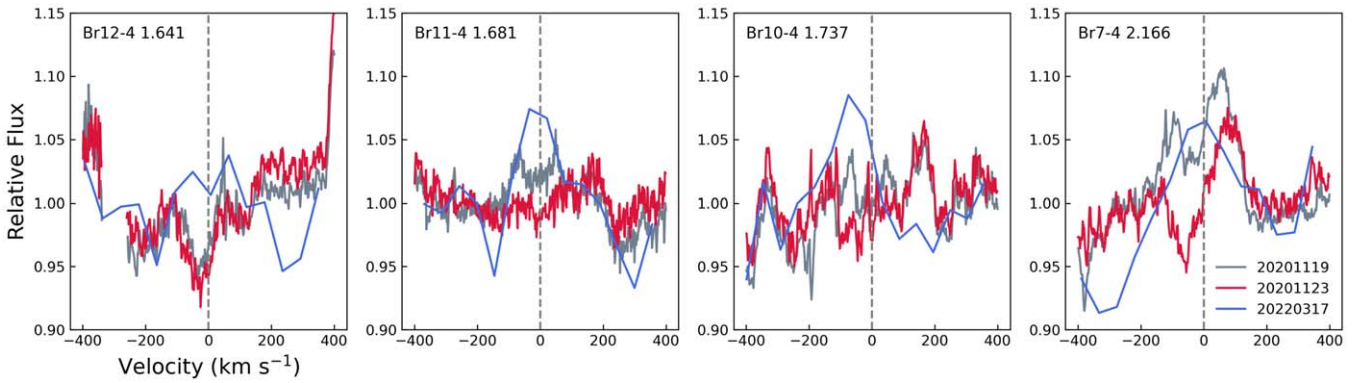
Figure 6. Observed Brackett series of Gaia19fct. Gray, red, and blue lines represent the data observed on 2020 November 19, 2020 November 23, and 2022 March 17, respectively.
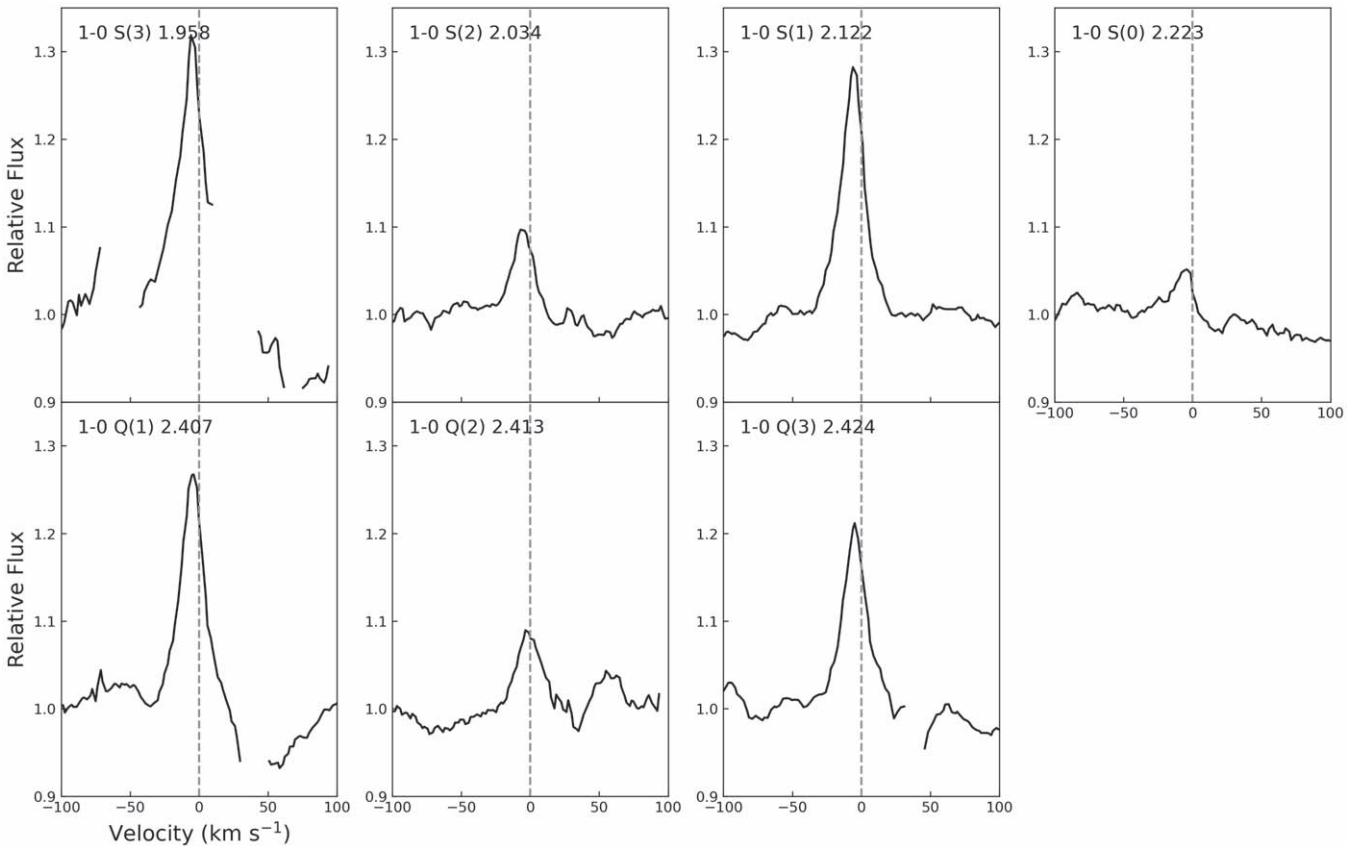

Figure 7. Observed H_2 lines in 2020 November. The part where the telluric correction is not perfect is missing, e.g., 1–0 S(3) 1.958 μm.

integration range, and then a 3σ criterion was used for the integration. EW was estimated with a Monte Carlo method with random Gaussian errors multiplied by the observation errors. The EW of each line was measured 100 times, and the standard deviation of all measurements was adopted as the uncertainty of the EW. In the case of the Br series observed on 2020 November 19 and 23, the EW was measured for both spectra since these Br series only varied between two IGRINS observations. We used the weighted mean spectrum of 2020 November for the other lines, which did not vary between the two observations. Measured EWs are listed in Table 5.

4.4.2. Brackett Series

Four Br series lines are observed in emission (Figure 6), where the H I emission lines are typically found in EXors (Lorenzetti et al. 2009). The Br lines are the only ones that show variation between the two IGRINS observations; therefore, we measured the EWs of each line (Section 4.4.1 and Table 5). The strengths of these lines on 2020 November 23 are weaker than in the spectrum taken 4 days earlier. Especially, the blueshifted absorption component of Brγ became stronger, indicating that the strength of wind increased within 4 days. The Br 12–4 and Br 10–4 lines are marginally detected in the 2020 November observations but observed firmly in 2022
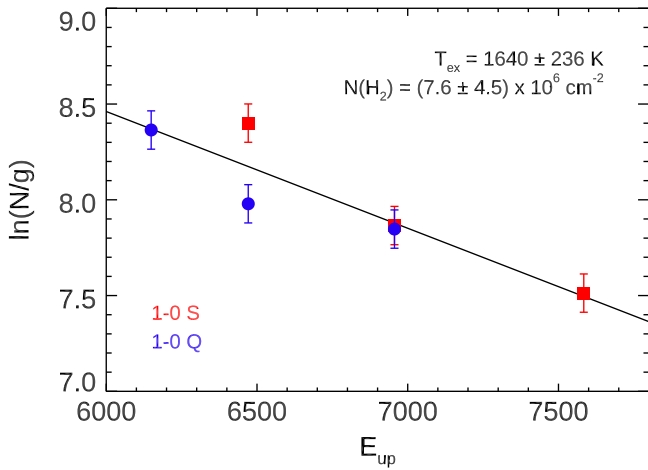
Figure 8. Excitation diagram of H_2.

March. The EW of the Br 11–4 increased in 2022, while the EW of the Brγ decreased in 2022. The EW of observed spectral lines varies depending on the observation epoch. These spectral line variations are consistent with previous studies (Hillenbrand 2019; Giannini et al. 2022), which show different line profiles depending on the brightness of Gaia19fct.

4.4.3. H_2 Lines

Several H_2 emission lines were observed in 2020 November (Figure 7), which are rarely detected in FUors or EXors. Only about 10% of eruptive stars showed H_2 rovibrational transitions: V1647 Ori (Aspin 2011), PTF 10nvg (Hillenbrand et al. 2013), Gaia19ajj (Hillenbrand et al. 2019), V960 Mon (Park et al. 2020), Gaia19bey (Hodapp et al. 2020), V346 Nor (Kóspál et al. 2020), and V899 Mon (Park et al. 2021a). The mean and standard deviation of the peak velocity is -5 ± 1 km s^{-1}, slightly blueshifted with respect to the systemic velocity. This blueshifted velocity indicates that these lines are formed by an outflowing wind (van den Ancker et al. 1999; Fernandes 2000; Nisini et al. 2002; Davis et al. 2003, 2010, 2011; Bally et al. 2007; Greene et al. 2010; Bally 2016).

We constructed an excitation diagram (Figure 8) to estimate the gas excitation temperature (T_{ex}) and the column density (N_{H2}) of H_2 lines (van den Ancker et al. 1999; Fernandes 2000; Nisini et al. 2002; Davis et al. 2011; Oh et al. 2018; Park et al. 2021a). The excitation diagram can be fitted by a single straight line if the gas is thermalized with a single temperature. T_{ex} can be obtained by the reciprocal slope of the fitted line, and the y-intercept can be used to calculate the N_{H2}. For this analysis, we adopted the $A_V = 8 \pm 1$ mag, and the line flux and line flux uncertainty were measured using the same method as EW. The estimated uncertainty of the line flux is about 1%, which might be underestimated. We considered the possible uncertainties of A_V, continuum fitting, and telluric correction and then assumed a 10% uncertainty for the line flux. In addition, we used only six lines, excluding the 1–0 $S(3)$ 1.958 μm line located in the crowded telluric region. The obtained T_{ex} and N_{H2} are 1640 ± 236 K and $(7.6 \pm 4.5) \times 10^6$ cm^{-2}, respectively. The obtained T_{ex} is lower than found for other eruptive young stars (V346 Nor and V899 Mon; Kóspál et al. 2020; Park et al. 2021a), suggesting that the T_{ex} of the shock-heated region in Gaia19fct is lower than in these two targets.

4.4.4. [Fe II] Lines

Figure 9 shows the comparison of forbidden [Fe II] lines observed in 2020 November (black) and 2022 March (blue). The [Fe II] lines in the second epoch became stronger and faster than in the first epoch, except for the [Fe II] 1.644 μm line. The mean and standard deviation of the peak velocities of the first and second epochs are -81 ± 2 km s^{-1} and -110 ± 59 km s^{-1}, respectively. It is hard to compare these lines quantitatively because of the lower S/N and spectral resolution of the second epoch. However, these line variations suggest that the physical properties of jets changed between the two epochs.

The electron density (n_e) and electron temperature (T_e) of the jet/outflow region can be estimated using the [Fe II] line ratios. To estimate the physical properties of the jet/outflow region, we only used the reliable first-epoch IGRINS spectrum, which has a higher S/N. We used a line ratio (log([Fe II] 1.644/1.534) = 0.40) of Nisini et al. (2002) and compared it with their Figure 8. The calculated ratio implies that n_e and T_e are higher than 10^5 cm^{-3} and 15,000 K, respectively. Then, we used the CHIANTI database[16] to calculate the model line ratios as done in Kóspál et al. (2020). Figure 10 shows the models and observed [Fe II] line ratios. The top panel ([Fe II] 1.534/1.644 = 0.397 ± 0.002) implies that n_e and T_e of Gaia19fct are higher than 10^5 cm^{-3} and 10,000 K, respectively, while the bottom panel ([Fe II] 1.600/1.644 = 0.191 ± 0.003) shows that n_e is between 10^4 and 10^5 cm^{-3}, but the temperature cannot be constrained using the observed line ratios because the model curves are degenerate. The obtained [Fe II] line ratios suggest that the jet/outflow region of Gaia19fct has n_e and T_e higher than 10^4 cm^{-3} and 10,000 K, respectively.

4.4.5. Metallic Lines

In addition to emission lines related to the accretion or jet/outflow, several metallic absorption lines are observed in 2020 November. Figure 11 shows relatively isolated and strong lines. The atomic metallic lines can form in a rotating disk or a protostellar photosphere. In the case of the FUors, the absorption-line profiles can form at a cooler disk photosphere seen in front of a hotter disk midplane, and the line profiles are double-peaked or boxy owing to the Keplerian rotation of the disk (Hartmann & Kenyon 1996; Fischer et al. 2022). The broad single-peaked line profiles can form at the rotating protostellar photosphere (Gray 1992). The observed NIR metallic lines show U-like or boxy profiles, similar to optical lines presented by Hillenbrand (2019), rather than a clear double-peaked profile. In order to investigate the origin of the metallic lines, we fitted these atomic absorption lines with the standard stellar spectrum from the IGRINS Spectral Library (Park et al. 2018) by convolving with disk rotational and stellar rotational profiles described in Yoon et al. (2021).

Most of the observed lines are blended with adjacent lines compared to the convolved stellar spectrum, making only three lines available for the fitting. The best fit was found by χ^2 minimization, and Figure 12 shows the best-fit results for the Mg I 1.574, Mg I 1.575, and Fe I 1.580 μm lines. The wavelengths of the three lines are close to each other; therefore, the same temperatures and spectral types are expected within the uncertainties. Due to the small number of lines used and the limited grid of spectral types and luminosity classes for
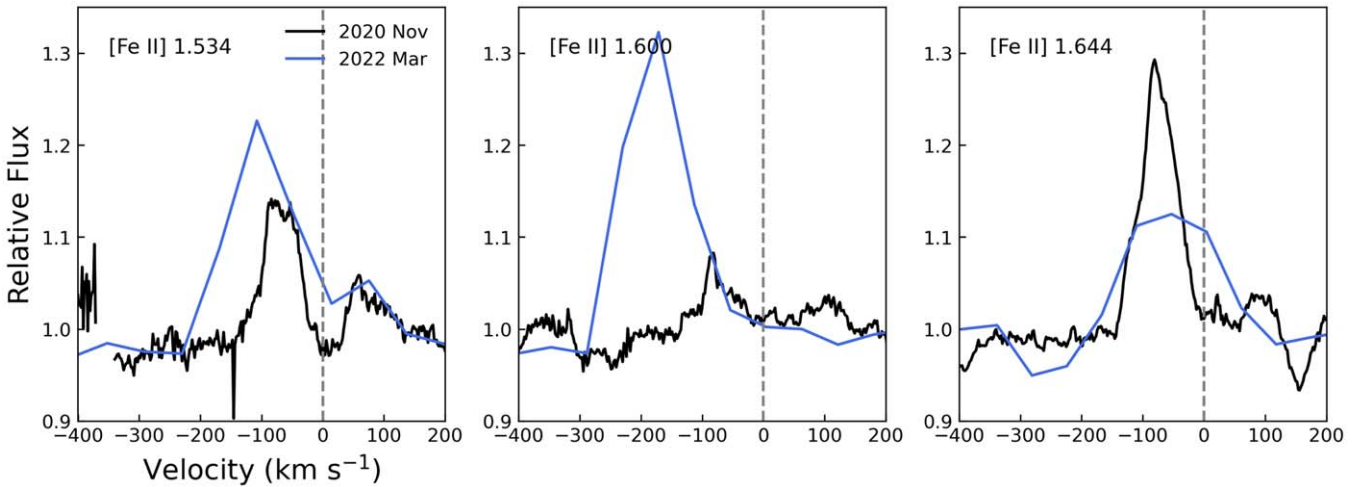
---

[16] http://chiantidatabase.org

Figure 9. [Fe II] emission lines observed in Gaia19fct. Black and blue lines present the spectrum observed in 2020 November and 2022 March, respectively.
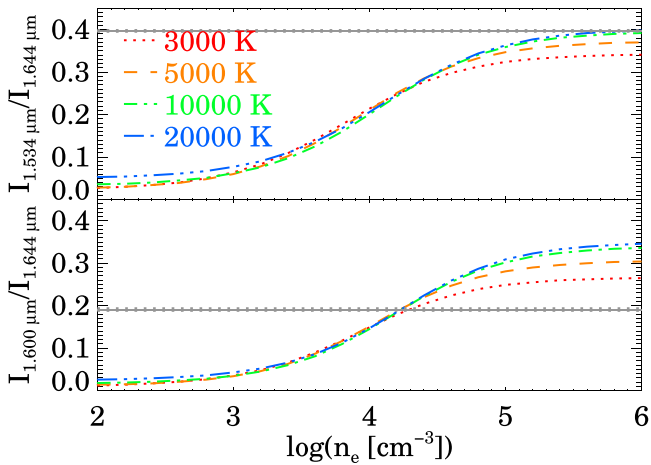

Figure 10. Observed [Fe II] line ratios for Gaia19fct. Dotted red, dashed orange, dashed–dotted green, and dashed–triple-dotted blue lines present models with $T_e = 3000$, 5000, 10,000, and 20,000 K, respectively. Gray horizontal lines and ticks represent the observed line ratios and uncertainties.

standard stars, we provide the ranges of spectral types and rotational velocities. The observed NIR lines are well fitted by a relatively cooler temperature (from K7 V to M5 V) with lower velocities (between 27 and 33 km s^{-1}) compared to the optical lines (F5 to G0 depending on luminosity class and about 70 km s^{-1}; Hillenbrand 2019). Additionally, the boxy profiles are better fitted with disk rotational profiles. This result shows the wavelength-dependent spectral type, typical of FUors, and suggests that these NIR metallic lines are formed at the cooler outer part of the disk in Keplerian rotation.

4.4.6. Stellar and Accretion Parameters

The estimation of the stellar parameters for embedded Class I objects is quite challenging, since they are difficult to observe in the visible. As a consequence, the spectral typing is limited to the NIR regime, where the contamination due to the extinction and the veiling is not negligible. The embedded nature of protostars is also a limitation to the direct estimate of the accretion luminosity because the Balmer jump in the near-UV is unobservable in them. This prevents us from studying stellar and accretion parameters of Class I YSOs using the same methods as used for Class II stars based on Balmer jump, absorption lines, and spectral shape (see, e.g., Manara et al. 2013, for spectral typing in Class II YSOs).

We estimated stellar parameters and accretion luminosity of Gaia19fct by modifying a self-consistent method usually used for Class I and flat-spectrum YSO analysis (Antoniucci et al. 2008; Fiorellino et al. 2021). This method is based on the following assumptions: (i) the bolometric luminosity is the sum of the stellar and the accretion luminosity ($L_{\rm bol} = L_\star + L_{\rm acc}$); (ii) the absolute bolometric magnitude in K band is $M_{\rm bol} = {\rm BC}_K + m_K + 2.5 \log(1 + r_K) - A_K - 5 \log(d/10 \,{\rm pc})$; and (iii) the empirical relations between the luminosity of H I lines and accretion luminosity found for classical T Tauri stars (CTTSs) are a good approximation for Class I stars (Nisini et al. 2005), in particular the one regarding the Brγ line, $\log L_{\rm acc} = a \log L_{{\rm Br}\gamma} + b$, where $a = 1.19 \pm 0.10$ and $b = 4.02 \pm 0.51$ (Alcalá et al. 2017). All these equations depend on the extinction. This method typically takes the measured H I flux, estimation of veiling, distance, and bolometric luminosity as input. Output includes extinction, stellar mass, radius, luminosity, spectral type (resulting from the bolometric correction ${\rm BC}_K$), and accretion luminosity.

Since this approach is valid for accreting objects until the magnetospheric accretion scenario works (Antoniucci et al. 2008; Fiorellino et al. 2021), we checked whether the spectrum we used for this analysis corresponds to a quiescent phase. Looking at Figure 3, we see that this condition is satisfied only for the NOTCam spectrum observed in 2022, as the two earlier spectra were taken during the fading phase of a brightening event. Moreover, since we need the estimation of the flux, contemporary photometry is also required. For this epoch, we have simultaneous photometric observation. We calculated the flux of the Brγ line by using the contemporary photometry in K band, $m_K = 10.476 \pm 0.009$ mag, obtaining $F_{{\rm Br}\gamma} = (3.89 \pm 0.06) \times 10^{-15}$ erg s^{-1} cm^{-2}. We adopted the distance of 0.92 kpc (Section 3.1) and $L_{\rm bol}$ of $5.6 \, L_\odot$ as we computed in Section 4.1. We assumed ages of 10^4 yr (birth line) and 1 Myr since the age of this source is unknown. Then, stellar parameters that satisfied equation (i) and located near the birth line and the 1 Myr line were found. Since we were not able to compute the veiling for this target, we set it as a free parameter, varying its value from 0 to 20, with steps of 0.1, looking for the set of
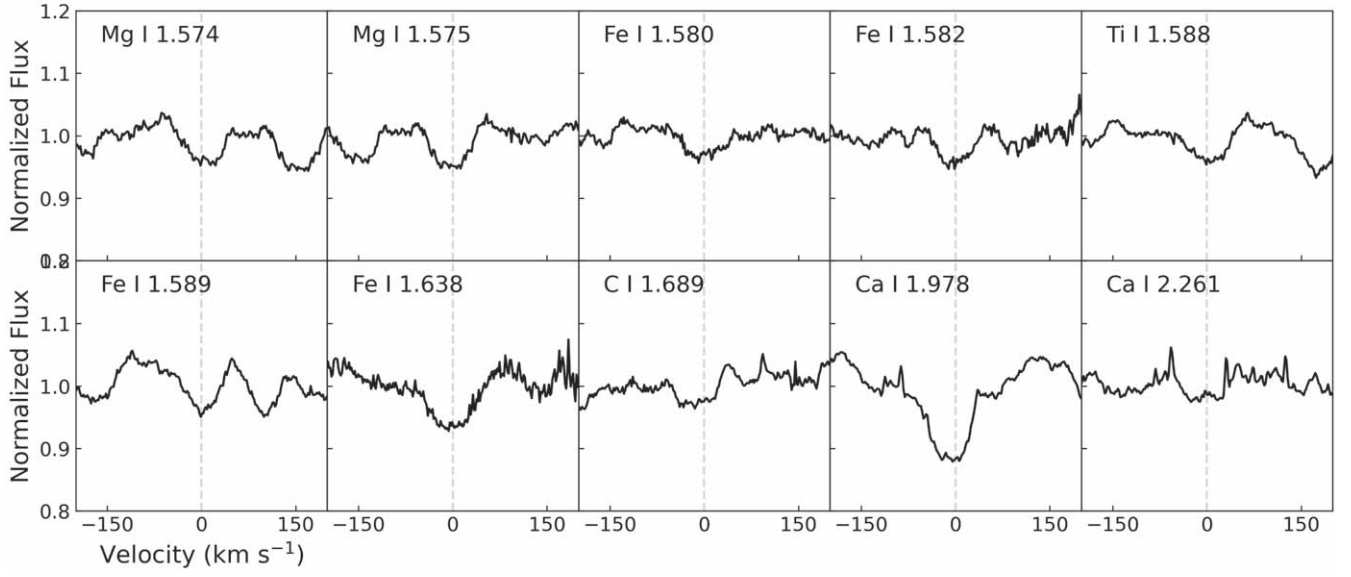
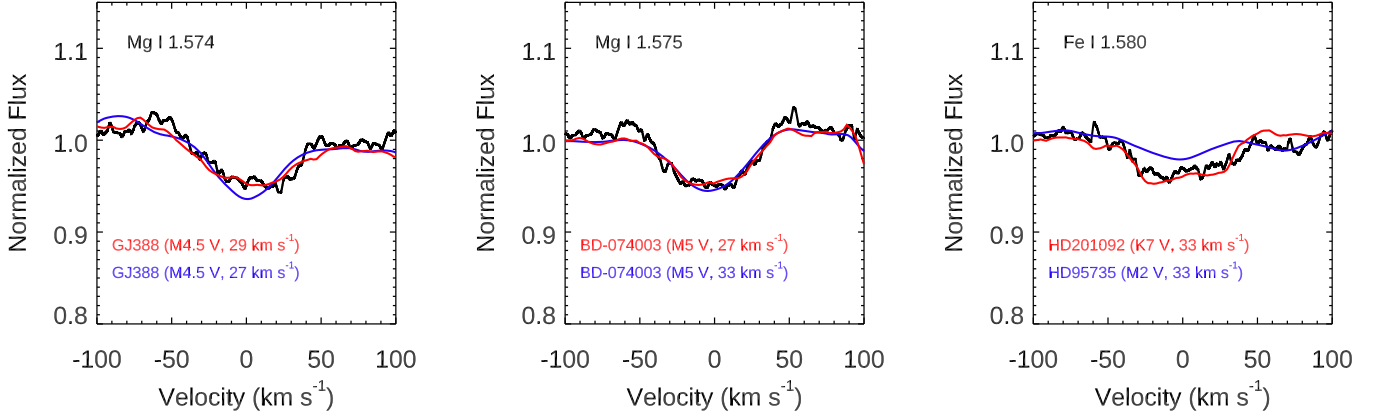**Figure 11.** Detected metallic absorption lines in 2020 November.

Figure 12. Best-fit results of Mg I 1.574, Mg I 1.575, and Fe I 1.580 μm. The black line shows the error-weighted mean spectrum of Gaia19fct. Red and blue lines present disk and stellar rotational profiles, respectively.

parameters in agreement with our extinction estimate, i.e., $A_V = 8 \pm 1$ mag (Section 4.2). As a result, we obtained the veiling (r_K), stellar mass (M_*), radius (R_*), and luminosity (L_*) that satisfy equations (i), (ii), and (iii) using the $F_{Br\gamma}$, L_{bol}, and A_V that we measured. The obtained values are listed in Table 6.

From these parameters, we computed the mass accretion rate ($\dot{M}_{acc}$) using

$$\dot{M}_{acc} = \left(1 - \frac{R_*}{R_{in}}\right)^{-1} \frac{L_{acc} R_*}{GM_*}, \qquad (4)$$

where R_{in} is the disk inner radius and assumed to be $5R_*$ (Hartmann et al. 1998). The calculated $\dot{M}_{acc}$ for the birth line and 1 Myr are $(2.1–2.6) \times 10^{-7}\ M_\odot\ \mathrm{yr}^{-1}$ and $(1.2–1.5) \times 10^{-7}\ M_\odot\ \mathrm{yr}^{-1}$, respectively, which are lower than typical for FUors, while similar to EXors or CTTSs (Fischer et al. 2022, and references therein). In addition, the obtained $\dot{M}_{acc}$ is compatible with Class I sources in the NGC 1333 cluster (see Figure 12 in Fiorellino et al. 2021), consistent with the evolutionary stage of Gaia19fct. One should keep in mind that our method is valid assuming magnetospheric accretion, resulting in the calculated

Table 6
Stellar and Accretion Parameters

Parameter	Birth Line (10^4 yr)	1 Myr
r_K	0.7–1.1	1.0–1.5
Spectral type	M1	K7
T_{eff} (K)	3631	3981
L_* ($L_\odot$)	5.16 ± 0.41	5.05 ± 0.12
M_* ($M_\odot$)	0.44 ± 0.01	0.70 ± 0.01
R_* ($R_\odot$)	5.26 ± 0.21	4.67 ± 0.19
L_{acc} ($L_\odot$)	0.50 ± 0.06	0.50 ± 0.06
$\dot{M}_{acc}$ ($10^{-7}\ M_\odot\ \mathrm{yr}^{-1}$)	2.10–2.63	1.17–1.47

mass accretion rate being a lower limit in the case of the eruptive stars. Additionally, veiling was found as a free parameter; therefore, a detailed study about veiling is needed for a more accurate estimate of the accretion rate. The average errors on the accretion luminosity, stellar radius, and mass are 0.4, 0.6, and 0.1 dex, respectively, which result in a cumulative error for the mass accretion rate of 0.8 dex.
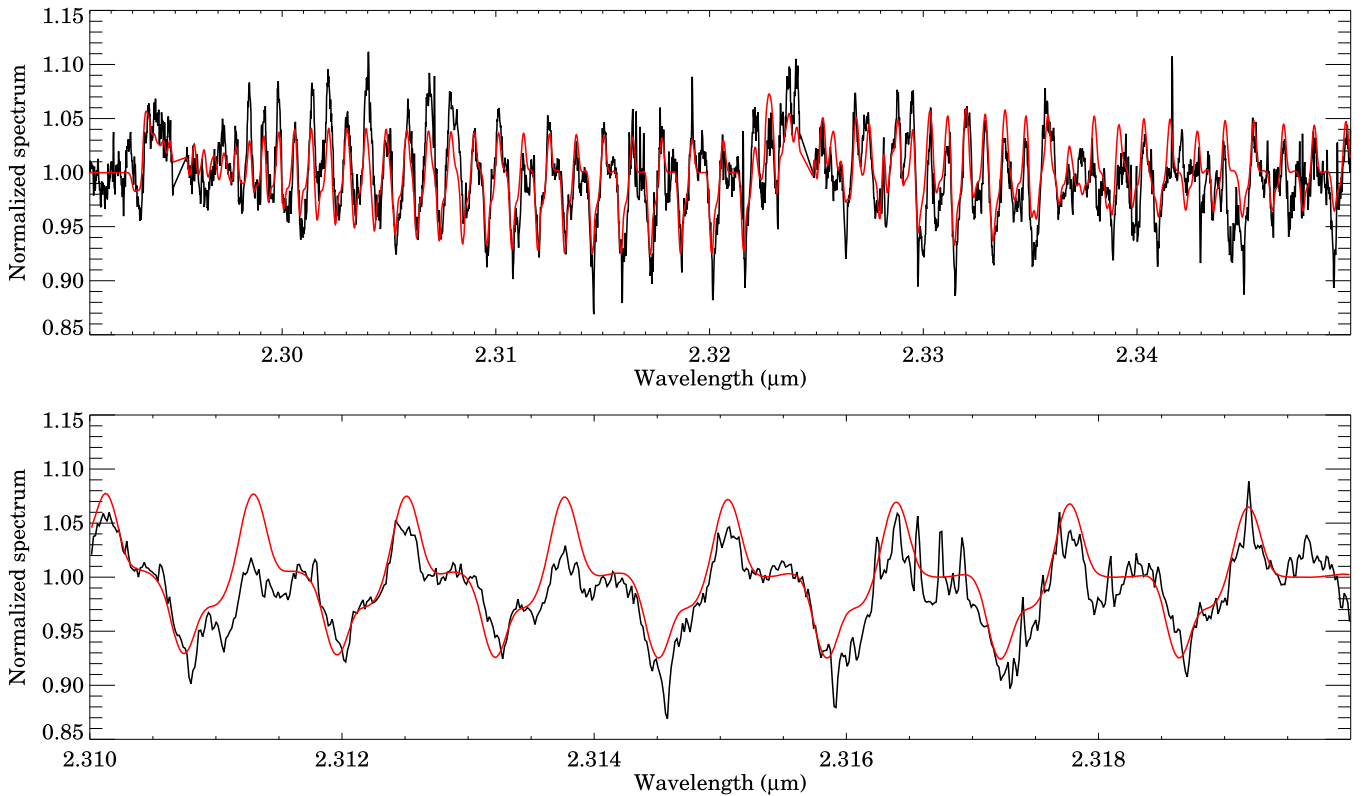
Figure 13. CO overtone features of Gaia19fct as observed on 2020 November 23. The black line shows the spectrum of Gaia19fct, and the red line represents the best-fit result. The top panel shows the full $v = 2 - 0$ and $v = 3 - 1$ series of lines, while the bottom panel is a zoom-in for some of the individual rotational transitions, clearly displaying the emission and two absorption components that make up the spectrum of Gaia19fct.

4.4.7. CO Modeling

The CO overtone feature in Gaia19fct appears to be a superposition of absorption and emission components, unlike what is typical in other young eruptive stars or T Tauri stars. The high spectral resolution of IGRINS allowed us to resolve the individual rotational lines of this feature. To determine the velocities of each component, we first normalized each rotational line of the $v = 2 - 0$ transition and took their mean. Then, we fitted Gaussian functions to this mean line profile. We found that the profile is best fitted with the sum of an emission component at $7.0 \, \mathrm{km \, s^{-1}}$ and two absorption components at -29.8 and $-60.5 \, \mathrm{km \, s^{-1}}$. This solution matches the mean $v = 3 - 1$ line profile as well, but we did not do a separate fit for it because of its lower S/N. The velocities given here are relative to the systemic velocity of $V_{\mathrm{LSR}} = 13.25 \, \mathrm{km \, s^{-1}}$ of Gaia19fct.

The varying ratio of the emission and absorption components suggested that the temperature and column density of the emitting and absorbing material are different. To quantify this, we used a simple isothermal slab model to calculate the expected CO overtone feature spectrum for a grid of different excitation temperatures (T) and CO column densities (N_{CO}), following the approach described in Kóspál et al. (2011) and Park et al. (2021a). For this analysis, we fitted both IGRINS spectra separately to provide ranges of the obtained physical parameters. The velocities of the three components were fixed to the values determined above. For simplicity, we also prescribed that T and N_{CO} are the same for the two absorption components. Thus, we had four free parameters in our fitting: T(emission), N_{CO}(emission), T(absorption), and N_{CO}(absorption). We found the minimal χ^2 with T(emission) $= 4100 \, \mathrm{K}$, N_{CO}(emission) $= 3.5 \times 10^{21} \, \mathrm{cm^{-2}}$, T

(absorption) $= 1200 \, \mathrm{K}$, and N_{CO}(absorption) $= 2.2 \times 10^{21} \, \mathrm{cm^{-2}}$ for the spectrum taken on 2020 November 19 and T(emission) $= 3200 \, \mathrm{K}$, N_{CO}(emission) $= 4.0 \times 10^{21} \, \mathrm{cm^{-2}}$, T(absorption) $= 1300 \, \mathrm{K}$, and N_{CO}(absorption) $= 2.8 \times 10^{21} \, \mathrm{cm^{-2}}$ for the spectrum taken on 2020 November 23. The latter spectrum and the corresponding model are shown in Figure 13.

Because the two IGRINS spectra taken 4 days apart agree well within the measurement uncertainties, the difference in the fitted parameters for the two spectra can be regarded as a confidence interval. Therefore, we conclude that the CO-emitting material is hotter, in the 3200–4100 K range, while the CO-absorbing material is cooler, in the 1200–1300 K range. Similarly, the CO-emitting material is optically thicker, with column densities in the $(3.5$–$4.0) \times 10^{21} \, \mathrm{cm^{-2}}$ range, while the CO-absorbing material is optically thinner, in the $(2.2$–$2.8) \times 10^{21} \, \mathrm{cm^{-2}}$ range.

Composite CO spectra, with the superposition of absorption and emission components at various velocities, are rarely seen in any kind of astronomical object. In the following, we discuss a few such examples we found in the literature, which may help us interpret what we see in Gaia19fct. Geballe et al. (2007) observed the highly variable composite CO overtone feature in the luminous red nova V838 Mon, where the absorption is interpreted as partly coming from the stellar photosphere, partly from high-velocity gas ejected by the outburst. Gorlova et al. (2006) detected a composite structure for the CO overtone band in the pulsating yellow hypergiant ρ Cas, with both the emission and the absorption components variable. Here, the different components originate in different atmospheric layers. Harrison (2016) observed the cataclysmic variable WZ Sge and found that its CO overtone feature has a central dip of

15

absorption superimposed on emission. In this case, the absorption is coming from a substellar L-dwarf companion, while the emission comes from the accretion disk of a white dwarf primary. Brittain et al. (2005) observed the fundamental CO lines toward the heavily embedded young star HL Tau and found narrow central absorption superimposed on broad emission with the same central velocity. The broad CO emission originates from the hot ($T \sim 1500$ K) inner disk, while the narrow absorption is caused by a large column of cold ($T \sim 100$ K) material.

None of the models or explanations found in the literature can be directly applied to Gaia19fct. Both the emission and absorption components here are relatively narrow (in the 8–12 km s^{-1} range, while the instrumental line broadening is 7 km s^{-1}). Therefore, it is unlikely that the emission is coming from the hot inner accretion disk, as usual with YSOs with high accretion rates. Instead, our results suggest that the emission might come from a slow, dense stellar wind with a high mass loss rate (Carr 1989). The blueshifted absorption components suggest multiple, expanding circumstellar shells, possibly launched by the stellar or disk wind.

5. Discussion

Gaia19fct has been studied in several works (Miller et al. 2015; Hillenbrand 2019; Giannini et al. 2022) after its discovery in 2015 (Miller et al. 2015). Since 2015, at least five burst events have occurred, and each of these events shows a different amplitude, duration, and speed of brightness variation (Δ mag/Δt; Section 4.3.1), indicating that, similar to the classical EXor V1118 Ori (Giannini et al. 2020), these bursts are not the periodic repetition of the same event. This is supported by the fact that the light curves of Gaia19fct do not present any clear periodicity on both large and small timescales (Section 4.3.2).

Sewiło et al. (2019) fitted the SED with a star and disk-only system and provided the best-fit results: $T_{\rm eff} \sim 9620$ K, $L_* \sim 111 \, L_\odot$, $M_* \sim 3 \, M_\odot$, $R_* \sim 3.8 \, R_\odot$, and Age ~ 2.13 Myr. These stellar parameters are not only higher than most of the FUors studied by Gramajo et al. (2014), including an intermediate-mass eruptive star Z CMa, but also higher than Class I sources studied by Fiorellino et al. (2021). In addition, according to our classification (Section 4.1) and previous studies (Miller et al. 2015; Fischer et al. 2016), Gaia19fct is classified as Class I rather than a star and disk-only system, which is more evolved. Therefore, we revisited the stellar parameters by modifying the self-consistent method described in Fiorellino et al. (2021) and provided the results in Table 6. The obtained parameters are in agreement with FUors (Gramajo et al. 2014) and Class I sources (Fiorellino et al. 2021).

5.1. Comparison with FUors

In our NIR spectra, we observed boxy or U-shape absorption-line profiles typically found in the Keplerian rotating disk of FUors. We fitted these lines by convolving the spectra of standard stars with disk rotational profiles and found the best-fit results (Section 4.4.5). The estimated rotational velocity is smaller than those of optical lines (Hillenbrand 2019), and the best-fit spectral type is also later than the optical spectrum (Hillenbrand 2019). These results suggest that Gaia19fct has a Keplerian rotating disk. If this

target has a Keplerian disk, the temperature and rotational velocity decrease with the radial extension of the disk (Fischer et al. 2022, and references therein). With the obtained rotational velocities, we estimated the location of the disk where these observed lines are formed by assuming an inclination of 90° and a stellar mass of $0.7 \, M_\odot$. We adopted the stellar mass obtained by assuming 1 Myr, which is more reasonable for Class I (Fiorellino et al. 2021), based on our classification (Section 4.1). For the optical lines, we adopted the rotational velocity (70 km s^{-1}) and spectral type (F0–G0 supergiants to dwarfs) from Hillenbrand (2019). Then, we assumed the temperature of 6359 K as the median spectral type of F5 V star HD 87141 (6359 K; Prugniel et al. 2011). For the NIR lines, we used the mean velocity of 30 km s^{-1} from our estimation (Section 4.4.5) and assumed the mean temperature of 3650 K between K7 V star HD 201092 (3911 K; Prugniel et al. 2011) and M5 V star BD –07°4003 (3209 K; Santos et al. 2013).

If we assume the disk inclination of 90° ($V_{\rm max} = v \sin i$) and stellar mass of $0.7 \, M_\odot$, the observed optical and NIR boxy or U-shape absorption lines trace $27 \pm 4 \, R_\odot$ and $148 \pm 21 \, R_\odot$ of the disk, respectively, and the temperature of the disk decreases from 6359 K at $27 \pm 4 \, R_\odot$ to 3650 K at $148 \pm 21 \, R_\odot$. Spectral features at shorter wavelengths trace the hotter inner part of the disk with higher rotational velocity. In comparison, the features at longer wavelengths trace the cooler outer part of the disk with lower rotational velocity. This result is consistent with the Keplerian rotating disk profile of FUors, including HBC 722 (Lee et al. 2015) and V960 Mon (Park et al. 2020). We also estimated the location of the disk traced by various spectral features for the prototype FU Ori by using the literature values listed in Table 7. The estimated radial distances traced by optical and NIR lines are about $18 \pm 3 \, R_\odot$ and $59 \pm 10 \, R_\odot$, respectively. Since the inclination of Gaia19fct is unknown, we calculated the disk radius by varying disk inclination, as shown in Figure 14. Depending on the inclination, the observed lines trace different radii. If the disk inclination is higher than 45°, the observed NIR lines of Gaia19fct trace a larger disk radius than those of three FUors. In contrast, optical lines trace a smaller disk radius than V960 Mon and HBC 722 but trace a smaller or larger disk radius than FU Ori. If the disk inclination is smaller than 30°, optical and NIR lines trace a smaller disk radius than HBC 722 and FU Ori and still trace a smaller disk radius than V960 Mon in optical, but they trace a larger disk radius in NIR. Since the observed boxy or U-shape line profiles do not present clear double-peaked profiles, the disk inclination might not be high. To constrain the disk radius traced by observed lines precisely, further study of disk inclination is needed.

5.2. Comparison with EXors

Weak CO overtone band head features superimposed with absorption profiles were observed in 2020 November. The CO overtone emission features are typically found in EXors and EXor-like objects (Kóspál et al. 2011; Hodapp et al. 2019, 2020; Park et al. 2021a; Cruz-Sáenz de Miera et al. 2022a). To study the physical properties ($T_{\rm ex}$ and $N_{\rm CO}$) where these CO features are formed, we fitted a simple slab model for the emission and absorption components separately and found the best-fit results (Section 4.4.7). We compared the fitting result of the emission component, which is formed in the hot inner accretion disk, with the prototype EXors EX Lup and EXor-like object V899 Mon. The CO excitation temperature of

Table 7
Comparison with FUors

Wavelength	Mass ($M_\odot$)	Target	v_{max} (km s^{-1})	Spectral Type	Temperature (K)	Radius[a] ($R_\odot$)	References
Optical	0.70 ± 0.01	Gaia19fct	70	F0–G0 I–V	6359[b]	27 ± 4	1, 2
	0.75 ± 0.25	V960 Mon	40.3 ± 3.8	G2 II–III/G5 III	5308/5013	88 ± 32	3, 4, 5, 6
	$0.8 \sim 1.0$	HBC 722	70	G5 II	5090	39 ± 7	7, 8, 9, 10
	0.60	FU Ori	65 ± 5	F8–G4	6420	18 ± 3	11, 12
NIR	0.70 ± 0.01	Gaia19fct	30 ± 3	K7 V–M5 V	3650[c]	148 ± 21	
	0.75 ± 0.25	V960 Mon	36.3 ± 3.9	K1 III	4634	109 ± 40	3, 4, 13
	$0.8 \sim 1.0$	HBC 722	50	K5 Iab	3055	76 ± 13	7, 8, 9, 14
	0.60	FU Ori	36 ± 3	M		59 ± 10	10, 12

Notes.
[a] Radius was calculated by using the maximum projected velocity (v_{max}).
[b] We assumed the temperature of the F5 V star (HD 87141) because Hillenbrand ([2019](#)) suggested a spectral type between F0 and G0 depending on luminosity class.
[c] Mean temperature of the K7 V star (HD 201092) and M5 V star (BD –07°4003) was used.

References. (1) Hillenbrand [2019](#); (2) Prugniel et al. [2011](#); (3) Kóspál et al. [2015](#); (4) Park et al. [2020](#); (5) Liu et al. [2014](#); (6) Park et al. [2018](#); (7) Kóspál et al. [2016](#); (8) Gramajo et al. [2014](#); (9) Lee et al. [2015](#); (10) Kovtyukh [2007](#); (11) Pérez et al. [2020](#); (12) Zhu et al. [2009](#); (13) Wu et al. [2011](#); (14) Bakos [1971](#).
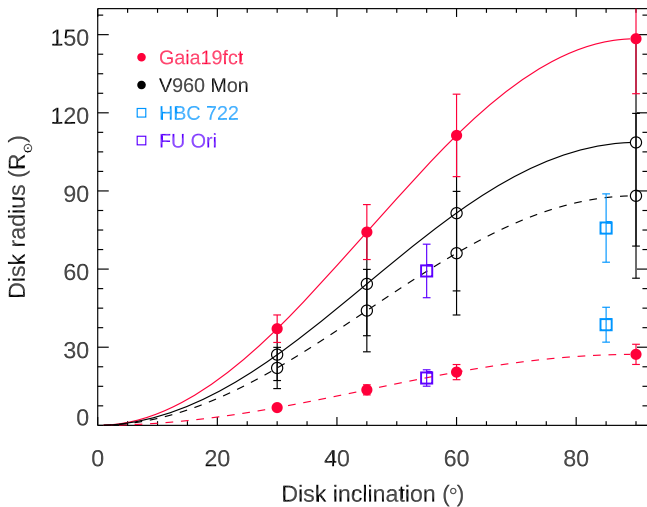
Figure 14. Calculated disk radius as a function of disk inclination. Different colors indicate different targets. Dashed and solid lines represent the radius calculated with the best-fit rotational velocity of optical and NIR lines (Table [7](#)), respectively. The circles represent the radius calculated with inclinations of 30°, 45°, 60°, and 90°.

Gaia19fct is higher (3200–4100 K) than those of EX Lup (2500 K; Kóspál et al. [2011](#)) and V899 Mon (2482 ± 326 K; Park et al. [2021a](#)), suggesting that the inner disk, where CO features are formed, of Gaia19fct is hotter than the two other objects.

6. Conclusions

We have conducted optical and NIR photometric and NIR spectroscopic observations of the young eruptive star Gaia19fct since 2016 September. We analyzed our observations along with public domain data to study the physical properties of Gaia19fct. From our analysis, our major conclusions are as follows.

1. Gaia19fct has been undergoing brightening events at least five times since its discovery in 2015 and keeps changing its brightness. The moderate amplitudes ($\Delta r = 2.5$–5 mag) and short timescales (<1 yr) of bursts are similar to EXors.

2. Overall gray variability from 2019 to 2022 suggests that a mechanism other than extinction change might cause the brightness variation.

3. We classified Gaia19fct using several methods: T_{bol}, α, and IR colors. T_{bol} and α suggest that the evolutionary stage of Gaia19fct is Class I, while the IR colors show Class I and flat spectrum. Based on our data, we suggest that Gaia19fct is in the Class I stage.

4. Our NIR spectra show both absorption and emission lines, similar to the characteristics of FUors and EXors, and the observed lines varied with time.

5. Several atomic metal lines are observed in absorption and well matched with K7−M5 dwarfs convolved with disk rotational profiles of about 30 km s^{-1}. This result agrees with the wavelength-dependent spectral type of FUors compared with those of the optical spectrum (Hillenbrand [2019](#)).

6. We calculated stellar and accretion parameters of Gaia19fct, finding that the stellar parameters are similar to low-mass, late-type stars, and the resulting mass accretion rate is more similar to EXors than to FUors.

7. The observed CO features have a composite structure of emission and absorption components, and our fitting result suggests that the emission is formed close to the star and the absorption is formed by expanding shells.

8. Our results show that Gaia19fct displays photometric and spectroscopic characteristics of both FUors and EXors, but it shows more similarity to EXors. The mixture of FUor and EXor properties is expected to provide important insights into our understanding of the accretion process in eruptive young stars. Therefore, further photometric and spectroscopic monitoring of Gaia19fct is needed.

ORCID iDs

Sunkyung Park https://orcid.org/0000-0003-4099-1171
Ágnes Kóspál https://orcid.org/0000-0001-7157-6275
Péter Ábrahám https://orcid.org/0000-0001-6015-646X
Fernando Cruz-Sáenz de Miera https://orcid.org/0000-0002-4283-2185
Eleonora Fiorellino https://orcid.org/0000-0002-5261-6216
Michał Siwak https://orcid.org/0000-0001-5018-3560
Zsófia Nagy https://orcid.org/0000-0002-3632-1194
Teresa Giannini https://orcid.org/0000-0002-7035-8513
Roberta Carini https://orcid.org/0000-0003-1604-2064
Zsófia Marianna Szabó https://orcid.org/0000-0001-9830-3509
Jeong-Eun Lee https://orcid.org/0000-0003-3119-2087
Jae-Joon Lee https://orcid.org/0000-0003-0894-7824

Fabrizio Vitali https://orcid.org/0000-0001-8332-4227
Mária Kun https://orcid.org/0000-0002-7538-5166
Máté Krezinger https://orcid.org/0000-0002-8813-4884
Levente Kriskovics https://orcid.org/0000-0002-1792-546X
András Pál https://orcid.org/0000-0001-5449-2467
Róbert Szakáts https://orcid.org/0000-0002-1698-605X
Krisztián Vida https://orcid.org/0000-0002-6471-8607
József Vinkó https://orcid.org/0000-0001-8764-7832

References

Ábrahám, P., Chen, L., Kóspál, Á., et al. 2019, ApJ, 887, 156
Alcalá, J. M., Manara, C. F., Natta, A., et al. 2017, A&A, 600, A20
Antoniucci, S., Nisini, B., Giannini, T., & Lorenzetti, D. 2008, A&A, 479, 503
Aspin, C. 2011, AJ, 142, 135
Audard, M., Ábrahám, P., Dunham, M. M., et al. 2014, in Protostars and Planets VI, ed. H. Beuther et al. (Tucson, AZ: Univ. Arizona Press), 387
Baek, G., Pak, S., Green, J. D., et al. 2015, AJ, 149, 73
Bailer-Jones, C. A. L., Rybizki, J., Fouesneau, M., Mantelet, G., & Andrae, R. 2018, AJ, 156, 58
Bakos, G. A. 1971, JRASC, 65, 222
Bally, J. 2016, ARA&A, 54, 491
Bally, J., Reipurth, B., & Davis, C. J. 2007, in Protostars and Planets V, ed. B. Reipurth, D. Jewitt, & K. Keil (Tucson, AZ: Univ. Arizona Press), 215
Beck, T. L. 2007, AJ, 133, 1673
Brittain, S. D., Rettig, T. W., Simon, T., & Kulesa, C. 2005, ApJ, 626, 283
Carpenter, J. M., Hillenbrand, L. A., & Skrutskie, M. F. 2001, AJ, 121, 3160
Carr, J. S. 1989, ApJ, 345, 522
Chambers, K. C., Magnier, E. A., Metcalfe, et al. 2016, arXiv:1612.05560
Chen, H., Myers, P. C., Ladd, E. F., & Wood, D. O. S. 1995, ApJ, 445, 377
Cody, A. M., Stauffer, J., Baglin, A., et al. 2014, AJ, 147, 82
Connelley, M. S., & Greene, T. P. 2010, AJ, 140, 1214
Connelley, M. S., & Reipurth, B. 2018, ApJ, 861, 145
Cruz-Sáenz de Miera, F., Kóspál, Á., Ábrahám, P., et al. 2022a, ApJ, 927, 125
Cruz-Sáenz de Miera, F., Kóspál, A., Ábrahám, P., et al. 2022b, ApJ, submitted
Cutri, R. M., Skrutskie, M. F., van Dyk, S., et al. 2003, yCat, 2246, 0
Cutri, R. M., Wright, E. L., Conrow, T., et al. 2014, yCat, 2328, 0
Davis, C. J., Cervantes, B., Nisini, B., et al. 2011, A&A, 528, A3
Davis, C. J., Gell, R., Khanzadyan, T., Smith, M. D., & Jenness, T. 2010, A&A, 511, A24
Davis, C. J., Smith, M. D., Stern, L., Kerr, T. H., & Chiar, J. E. 2003, MNRAS, 344, 262
Dunham, M. M., Evans, N. J. I., Terebey, S., Dullemond, C. P., & Young, C. H. 2010, ApJ, 710, 470
Evans, C. J., Simard, L., & Takami, H. 2016, Proc. SPIE, 9908, 99080C
Evans, N. J. I., Dunham, M. M., Jørgensen, J. K., et al. 2009, ApJS, 181, 321
Evitts, J. J., Froebrich, D., Scholz, A., et al. 2020, MNRAS, 493, 184
Fedele, D., van den Ancker, M. E., Petr-Gotzens, M. G., & Rafanelli, P. 2007, A&A, 472, 207
Fernandes, A. J. L. 2000, MNRAS, 315, 657
Fiorellino, E., Manara, C. F., Nisini, B., et al. 2021, A&A, 650, A43
Fischer, W. J., Hillenbrand, L. A., Herczeg, G. J., et al. 2022, arXiv:2203.11257
Fischer, W. J., Padgett, D. L., Stapelfeldt, K. L., & Sewiło, M. 2016, ApJ, 827, 96
Froebrich, D., Campbell-White, J., Scholz, A., et al. 2018, MNRAS, 478, 5091
Gaia Collaboration, Vallenari, A., Brown, A. G. A., et al. 2022, arXiv:2208.00211
Geballe, T. R., Evans, A., van Loon, J. T., et al. 2007, in ASP Conf. Ser. 363, The Nature of V838 Mon and its Light Echo, ed. R. L. M. Corradi & U. Munari (San Francisco, CA: ASP), 110
Ghosh, A., Sharma, S., Ninan, J. P., et al. 2022, ApJ, 926, 68
Giannini, T., Giunta, A., Gangi, M., et al. 2022, ApJ, 929, 129
Giannini, T., Giunta, A., Lorenzetti, D., et al. 2020, A&A, 637, A83
Gorlova, N., Lobel, A., Burgasser, A. J., et al. 2006, ApJ, 651, 1130
Gramajo, L. V., Rodón, J. A., & Gómez, M. 2014, AJ, 147, 140
Gray, D. F. 1992, Sci, 257, 1978
Green, G. M., Schlafly, E., Zucker, C., Speagle, J. S., & Finkbeiner, D. 2019, ApJ, 887, 93
Green, J. D., Robertson, P., Baek, G., et al. 2013, ApJ, 764, 22
Greene, T. P., Barsony, M., & Weintraub, D. A. 2010, ApJ, 725, 1100
Gregorio-Hetem, J. 2008, in Handbook of Star Forming Regions, Volume II: The Southern Sky, ed. B. Reipurth (San Francisco, CA: ASP), 1
Hackstein, M., Haas, M., Kóspál, Á., et al. 2015, A&A, 582, L12

Harrison, T. E. 2016, ApJ, 816, 4
Hartmann, L., Calvet, N., Gullbring, E., & D'Alessio, P. 1998, ApJ, 495, 385
Hartmann, L., Herczeg, G., & Calvet, N. 2016, ARA&A, 54, 135
Hartmann, L., & Kenyon, S. J. 1996, ARA&A, 34, 207
Henden, A. A., Levine, S., Terrell, D., & Welch, D. L. 2015, AAS Meeting Abstracts, 225, 336.16
Herbig, G. H. 1977, ApJ, 217, 693
Herbig, G. H. 1989, in ESO Workshop on Low Mass Formation and Pre-Main Sequence Objects 33 (Garching: ESO), 233
Herbig, G. H. 2007, AJ, 133, 2679
Hillenbrand, L. A. 2019, ATel, 13321, 1
Hillenbrand, L. A., Contreras Peña, C., Morrell, S., et al. 2018, ApJ, 869, 146
Hillenbrand, L. A., Miller, A. A., Covey, K. R., et al. 2013, AJ, 145, 59
Hillenbrand, L. A., Reipurth, B., Connelley, M., Cutri, R. M., & Isaacson, H. 2019, AJ, 158, 240
Hodapp, K. W., Denneau, L., Tucker, M., et al. 2020, AJ, 160, 164
Hodapp, K. W., Reipurth, B., Pettersson, B., et al. 2019, AJ, 158, 241
Hodgkin, D., Harrison, T., Breedt, H., et al. 2021, A&A, 652, A76
Ishihara, D., Onaka, T., Kataza, H., et al. 2010, A&A, 514, A1
Kaltcheva, N. T., & Hilditch, R. W. 2000, MNRAS, 312, 753
Kanodia, S., & Wright, J. 2018, RNAAS, 2, 4
Kenyon, S. J., Hartmann, L. W., Strom, K. M., & Strom, S. E. 1990, AJ, 99, 869
Koenig, X. P., & Leisawitz, D. T. 2014, ApJ, 791, 131
Kóspál, Á., Ábrahám, P., Acosta-Pulido, J. A., et al. 2016, A&A, 596, A52
Kóspál, Á., Ábrahám, P., Goto, M., et al. 2011, ApJ, 736, 72
Kóspál, Á., Ábrahám, P., Moór, A., et al. 2015, ApJL, 801, L5
Kóspál, Á., Szabó, Z., Ábrahám, P., et al. 2020, ApJ, 889, 148
Kovtyukh, V. V. 2007, MNRAS, 378, 617
Kraus, S., Caratti o Garatti, A., Garcia-Lopez, R., et al. 2016, MNRAS, 462, L61
Lada, C. J. 1987, in IAU Symp. 115, ed. M. Peimbert & J. Jugaku (Cambridge: Cambridge Univ. Press), 1
Lawrence, A., Warren, S. J., Almaini, O., et al. 2007, MNRAS, 379, 1599
Lee, J.-E., Park, S., Green, J. D., et al. 2015, ApJ, 807, 84
Lee, J.-J., & Gullikson, K. 2017, igrins/plp v2.2.0-alpha.4, Zenodo, doi:10.5281/zenodo.438353
Liu, Y. J., Tan, K. F., Wang, L., et al. 2014, ApJ, 785, 94
Lorenzetti, D., Larionov, V. M., Giannini, T., et al. 2009, ApJ, 693, 1056
Lykou, F., Ábrahám, P., Chen, L., et al. 2022, A&A, 663, A86
Magakian, T. Y., Nikogossian, E. H., Movsessian, T., et al. 2013, MNRAS, 432, 2685
Mainzer, A., Bauer, J., Cutri, R. M., et al. 2014, ApJ, 792, 30
Mainzer, A., Bauer, J., Grav, T., et al. 2011, ApJ, 731, 53

Manara, C. F., Beccari, G., Da Rio, N., et al. 2013, A&A, 558, A114
Masci, F. J., Laher, R. R., Rusholme, B., et al. 2019, PASP, 131, 018003
Megeath, S. T., Gutermuth, R., Muzerolle, J., et al. 2012, AJ, 144, 192
Miller, A. A., Hillenbrand, L. A., Bilgi, P., et al. 2015, ATel, 7428, 1
Nisini, B., Antoniucci, S., Giannini, T., & Lorenzetti, D. 2005, A&A, 429, 543
Nisini, B., Caratti o Garatti, A., Giannini, T., & Lorenzetti, D. 2002, A&A, 393, 1035
Oh, H., Pyo, T.-S., Koo, B.-C., et al. 2018, ApJ, 858, 23
Park, S., Kóspál, Á., Cruz-Sáenz de Miera, F., et al. 2021a, ApJ, 923, 171
Park, S., Lee, J.-E., Kang, W., et al. 2018, ApJS, 238, 29
Park, S., Lee, J.-E., Pyo, T.-S., et al. 2020, ApJ, 900, 36
Park, W., Lee, J.-E., Contreras Peña, C., et al. 2021b, ApJ, 920, 132
Pérez, S., Hales, A., Liu, H. B., et al. 2020, ApJ, 889, 59
Petersen, L., & Gammelgaard, P. 1996, A&A, 308, 49
Prugniel, P., Vauglin, I., & Koleva, M. 2011, A&A, 531, A165
Ramsay, S. K., McLean, I. S., & Takami, H. 2014, Proc. SPIE, 9147, 91471D
Rieke, G. H., & Lebofsky, M. J. 1985, ApJ, 288, 618
Rigliaco, N. C., Gratton, S. G., Kóspál, Á., et al. 2020, A&A, 641, A33
Santos, N. C., Sousa, S. G., Mortier, A., et al. 2013, A&A, 556, A150
Sewiło, M., Whitney, B. A., Yung, B. H. K., et al. 2019, ApJS, 240, 26
Shu, F. H. 1977, ApJ, 214, 488
Siwak, M., Ogłoza, W., & Krzesiński, J. 2020, A&A, 644, A135
Siwak, M., Ruciński, S. M., Matthews, J. M., et al. 2013, MNRAS, 432, 194
Siwak, M., Winiarski, M., Ogłoza, W., et al. 2018, A&A, 618, A79
Szabó, Z., Kóspál, Á., Ábrahám, P., et al. 2021, ApJ, 917, 80
Szabó, Z., Kóspál, Á., Ábrahám, P., et al. 2022, ApJ, 936, 64
Szegedi-Elek, E., Ábrahám, P., Wyrzykowski, Ł., et al. 2020, ApJ, 899, 130
Takagi, Y., Honda, S., Arai, A., et al. 2018, AJ, 155, 101
Tody, D. 1986, Proc. SPIE, 627, 733
Turner, J., Kirby-Docken, K., & Dalgarno, A. 1977, ApJS, 35, 281
van den Ancker, M. E., Wesselius, P. R., Tielens, A. G. G. M., van Dishoeck, E. F., & Spinoglio, L. 1999, A&A, 348, 877
Vitali, F., McLean, I. S., Iye, M., et al. 2006, Proc. SPIE, 6269, 626954
Vitali, F., Zerbi, F. M., Chincarini, G., et al. 2003, Proc. SPIE, 4841, 627
Wright, E. L., Eisenhardt, P. R. M., Mainzer, A. K., et al. 2010, AJ, 140, 1868
Wu, Y., Singh, H. P., Prugniel, P., Gupta, R., & Koleva, M. 2011, A&A, 525, A71
Yoon, S.-Y., Lee, J.-E., Lee, S., et al. 2021, ApJ, 919, 116
Yuk, I.-S., McLean, I. S., Ramsay, S. K., et al. 2010, Proc. SPIE, 7735, 77351M
Zerbi, F. M., Chincarini, G., Rodonó, M., et al. 2001, in Gamma-ray Bursts in the Afterglow Era, ed. E. Costa, F. Frontera, & J. Hjorth (Berlin: Springer), 434
Zhu, Z., Espaillat, C., Hinkle, K., et al. 2009, ApJL, 694, L64